Drug-induced changes in connectivity to midbrain dopamine cells revealed by rabies monosynaptic tracing

Katrina Bartas[1], Pieter Derdeyn[1], Guilian Tian[2], Jose J. Vasquez[2], Ghalia Azouz[2], Cindy M. Yamamoto[2], May Hui[2], Kevin T. Beier[2-5]

1 Program in Mathematical, Computational, and Systems Biology. University of California, Irvine, Irvine, CA, USA 92697-4560
2 Department of Physiology and Biophysics, University of California, Irvine, Irvine, CA, USA 92697-4560
3 Department of Neurobiology and Behavior, University of California, Irvine, Irvine, CA, USA 92697-4560
4 Department of Biomedical Engineering, University of California, Irvine, Irvine, CA, USA 92697-4560
5 Department of Pharmaceutical Sciences, University of California, Irvine, Irvine, CA, USA 92697-4560

*Corresponding author
Contact information:
Kevin Beier
825 Health Sciences Road
Medical Sciences D337
Irvine, CA 92697
Phone: 949-824-1083
Email: kbeier@uci.edu

ABSTRACT:

Addictive drugs cause long-lasting changes in connectivity from inputs onto ventral tegmental area dopamine cells (VTA^{DA}) that contribute to drug-induced behavioral adaptations. However, it is not known which inputs are altered. Here we used a rabies virus (RABV)-based mapping strategy to quantify RABV-labeled inputs to VTA cells after a single exposure to one of a variety of misused drugs – cocaine, amphetamine, methamphetamine, morphine, and nicotine – and compared the relative global input labeling across conditions. We observed that all tested addictive drugs elicited similar input changes onto VTA^{DA} cells, in particular onto DA cells projecting to the lateral shell of the nucleus accumbens and amygdala. In addition, repeated administration of ketamine/xylazine to induce anesthesia induces a change in inputs to VTA^{DA} cells that is similar to but different from those elicited by a single exposure to addictive drugs, suggesting that caution should be taken when using ketamine/xylazine-based anesthesia in rodents when assessing motivated behaviors. Furthermore, comparison of viral tracing data to an atlas of gene expression in the adult mouse brain showed that the basal expression patterns of several gene classes, especially calcium channels, were highly correlated with the extent of both addictive drug- or ketamine/xylazine-induced changes in RABV-labeled inputs to VTA^{DA} cells. Reducing expression levels of the voltage-gated calcium channel *Cacna1e* in cells in the nucleus accumbens lateral shell reduced RABV-mediated input labeling of these cells into VTA^{DA} cells. These results directly link genes controlling cellular excitability and the extent of input labeling by RABV.

46 **INTRODUCTION:**

47 The ventral tegmental area (VTA) contains dopamine cells (VTA^{DA}) that play key roles in several
48 behavioral processes, including reward, aversion, and motor control[1–3]. VTA^{DA} cells are
49 heterogeneous, with recent studies identifying subpopulations of VTA^{DA} cells that differentially
50 contribute to adaptive and pathological behaviors[4–7]. Numerous studies have mapped the input-
51 output architecture of VTA cells generally, as well as subpopulations of constituent DAergic,
52 GABAergic, and glutamatergic cells[7–12]. These studies have helped us to understand the biased
53 input and discrete output logic of the VTA, as well as generate hypotheses regarding the function
54 of circuits including the VTA.

55

56 In addition to normal adaptive behaviors, VTA^{DA} cells critically contribute to a variety of behaviors
57 related to substance use disorder (SUD), including reward, sensitization, and withdrawal elicited
58 by addictive drugs[13–18]. For a variety of misused drugs, even a single exposure triggers long-
59 lasting changes in synaptic plasticity onto VTA^{DA} cells[19,20]. These changes include both a long-
60 lasting enhancement of excitatory synaptic strength onto VTA^{DA} cells[20], and development of
61 inhibitory synaptic plasticity[21,22]. These changes are essential for a variety of drug-induced
62 behaviors, linking plasticity at VTA^{DA} cells with downstream behavioral changes[22–24]. Furthermore,
63 the changes in excitatory synaptic plasticity specifically occur onto some cell types and not others[5],
64 indicating that these adaptations are likely cell type- and pathway-specific. However, it remains
65 unknown which sets of inputs are modified, and if these changes are consistent across misused
66 drugs. Furthermore, synaptic plasticity is not the only type of long-lasting change that can be
67 induced by addictive drugs. Unfortunately, even less is known about how other forms of
68 experience-dependent changes, including elevations in input activity, may contribute to addiction-
69 related behaviors.

70

71 We recently showed that a single dose of cocaine causes long-lasting changes in cellular activity
72 in inputs to VTA^{DA} cells[15,16]. These changes occur from the globus pallidus external segment (GPe)
73 and bed nucleus of the stria terminalis (BNST) projections to the VTA that contribute to drug-
74 induced reward and sensitization, or withdrawal anxiety, respectively[15,25]. Notably, while these
75 studies focused on inputs from the GPe and BNST, the viral mapping results also demonstrated
76 the existence of other input changes to the VTA that were not pursued in those studies. These
77 unexplored connections may provide critical information about how drugs alter connectivity onto
78 VTA^{DA} cells, which in turn contributes to drug-induced behavioral changes[15,16].

79

80 In this study, we explore the brain-wide changes in RABV-labeled inputs to VTA cells elicited by
81 a variety of different drugs, including addictive drugs, an anesthetic mixture of ketamine/xylazine
82 (K/X), and fluoxetine, a psychoactive but non-addictive control substance. Our study provides a
83 first-of-its-kind exploration into how even a single drug exposure can change brain-wide
84 connectivity patterns, in addition to highlighting some concerns about the potential effects of K/X
85 anesthesia on motivated behavior.
86
87 **MATERIALS AND METHODS:**
88 **Experimental Procedures**
89 Animals: Mice were housed on a 12-hour light–dark cycle with food and water ad libitum. Males
90 and females from a C57/BL6 background were used for all experiments in approximately equal
91 proportions. Mice were approximately 3-4 months of age at the time of experiments. All surgeries
92 were done under isoflurane or ketamine/xylazine anesthesia. All procedures complied with the
93 animal care standards set forth by the National Institute of Health and were approved by the
94 University of California, Irvine's Institutional Animal Care and Use Committee (IACUC).
95
96 Stereotaxic surgery: Mice were anesthetized with 3-4% isoflurane and maintained during surgery
97 at 1-1.5% isoflurane, or with a mixture of ketamine (100 mg/mL) and xylazine (5 mg/mL). Mice
98 were secured in a stereotaxic apparatus (Stoelting). Under aseptic conditions, guide holes were
99 drilled, and viruses were infused into the target sites using a glass capillary attached to a
100 microinjection pump (WPI, UMP3T). 100 nL of AAVs or 500 nL of EnvA-pseudotyped RABV were
101 infused at a rate of 1.6 nL/s. The glass capillary remained in place for 5 min following the infusion
102 to allow for virus diffusion. After infusion, the surgical incision sites were closed with either sutures
103 or Vetbond tissue adhesive (Patterson Veterinary). Vetameg (flunixin, Patterson veterinary) was
104 administered for pain management and topical bacitracin was applied to prevent infection at the
105 incision site.
106
107 For viral injections mapping experiments from a defined cell type, 100 nL of a 1:1 volume mixture
108 of AAV_5-CAG-FLEx^{loxP}-TCB and AAV_8-CAG-FLEx^{loxP}-RABV-G was injected into the VTA of DAT-
109 Cre[26], GAD2-Cre[27], or vGluT2-Cre mice[28]. Thirteen days later, animals were given a single
110 injection of an addictive drug, fluoxetine, or saline. The following day, 500 nL of EnvA-
111 pseudotyped RABV was injected into the VTA. Animals were sacrificed five days later. For cTRIO
112 experiments shown in **Figure 7**, during the first surgery AAV_5-CAG-FLEx^{FRT}-TCB and AAV_8-CAG-
113 FLEx^{FRT}-RABV-G were injected into the VTA, and CAV2-FLEx^{loxP}-Flp was injected into an output

114 site (NAcLat, Amygdala, NAcMed, mPFC) during the same surgery. All other procedures were
115 the same as above. RABV-labeled cells throughout the brain were manually quantified, as done
116 previously[7,10,15].
117
118 The injection coordinates and volumes used were as follows:
119 VTA: 100 nL AAV and 500 nL RABV, AP –3.2, LM 0.4, DV –4.2
120 NAcMed: 250 nL, AP +1.78, L0.4, DV –4.1
121 NAcLat: 250 nL, AP +1.45, LM 1.75, DV –4.0
122 Amygdala: 500 nL, AP –1.43, LM 2.5, DV –4.5
123 mPFC: 1 μL into mPFC (two injections of 500 nL, one at AP +2.15, LM 0.27, DV –2.1 and another
124 at AP +2.15, L0.27, DV –1.6
125
126 The titers of the viruses used, based on quantitative PCR analysis, were as follows:
127 AAV_5-CAG-FLEx^{loxP}-TC, 2.4 x 10^{13} genome copies (gc)/mL;
128 AAV_8-CAG-FLEx^{loxP}-G, 1.0 x 10^{12} gc/mL;
129 AAV_5-CAG-FLEx^{FRT}-TC, 2.6 x 10^{12} gc/mL;
130 AAV_8-CAG-FLEx^{FRT}-G, 1.3 x 10^{12} gc/mL;
131 CAV-FLEx^{loxP}-Flp, 5.0 x 10^{12} gc/mL.
132 The titer of RABVΔG was estimated to be 5.0 x 10^8 colony forming units (cfu)/mL based on serial
133 dilutions of the virus stock followed by infection of the 293-TVA800 cell line.
134
135 Drug administration: Cocaine was administered (intraperitoneal injections) at a dose of 15 mg/kg,
136 morphine at 10 mg/kg, methamphetamine at 2 mg/kg, amphetamine at 10 mg/kg, nicotine at 0.5
137 mg/kg, and fluoxetine at 10 mg/kg.
138
139 Quantification of RABV data: RABV mapping data were analyzed as described previously[7,10]. All
140 RABV mapping data included were previously published[7,10,15], except for input tracing from mice
141 treated with a single dose of methamphetamine. The SAD B19 vaccine stain was used for all
142 experiments. A total of 118 samples were included in this study (**Table 1**). Exclusion criteria
143 included mice in which fewer than 200 input cells were labeled, or in cases where injections were
144 mistargeted (e.g., starter cells in the substantia nigra pars compacta). Experimenters were blinded
145 to the experimental condition when data quantification was being performed. For starter cell
146 center of mass calculations, we mapped the distribution of starter neurons, as defined by TVA-

147 mCherry expression along the A-P axis, and in the sections at the center point along this axis,
148 defined the center of labeling in along the M-L axis.
149
150 **CRISPRi experiments**
151 Plasmid construction: The CRISPRi system was adapted from Kumar's method[29]. pJEP317
152 pAAV-U6SaCas9gRNA(SapI)-EFS-GFP-KASH-pA was obtained from Addgene and was used as
153 a template to clone pJEP317-pAAV-U6-Cacna1eAC-EFS-GFP-KASH-pA using the Q5 Site-
154 directed mutagenesis kit (primers: 5'-acctccgtaaGTTTTAGTACTCTGGAAACAG-3' and 5'-
155 atgaacccttGGTGTTTCGTCCTTTCCAC-3') to insert the gRNA sequence
156 (AAGGGTTCATACCTCCGTAA) for *Cacna1e*. The gRNA sequence was selected from the IDT
157 Predesigned Alt-R™ CRISPR-Cas9 guide RNA resource
158 (https://www.idtdna.com/site/order/designtool/index/CRISPR_PREDESIGN). The plasmid for
159 CRISPRi (pJEP309-pAAV-EFS-dSaCas9-KRAB-Dio-pA), pAAV2-8, and pAAV2-5 were obtained
160 from Addgene. pHelper plasmid was a gift from Matthew Banghart at the University of California,
161 San Diego.
162
163 AAV production, purification, and titering: Generation of AAVs from plasmids and AAV Purification
164 by Iodixanol Gradient Ultracentrifugation were carried out as described on Addgene's
165 website with minor modifications. Briefly, pHelper, pAAV2-5/pAAV2-8 and pJEP309/pJEP317-
166 pAAV-U6-Cacna1eAC-EFS-GFP-KASH-pA plasmids were transfected into HEK293T cells using
167 PEIMAX (Polysciences, cat# 24765-100). The molar ratio for pHelper:pAAV2-5:transfer plasmid
168 was 1:1:1, and the ratio of total plasmids to PEIMAX was 1:3. 72 hrs post-transfection, cell lysate
169 and medium precipitated with PEG were purified by iodixanol gradient. Purified AAVs were titered
170 using primers against viral ITRs (5'-GGAACCCCTAGTGATGGAGTT-3' and 5'-
171 CGGCCTCAGTGAGCGA-3').
172
173 Viral injection: Prior to surgery, DAT-Cre mice were anesthetized with isoflurane (4% induction,
174 1-1.5% maintenance) and secured on a stereotaxic frame for precise localization of injection sites.
175 For assessment of *in vivo* genome editing, two conditions were generated. For the experimental
176 condition, 600 nL of a 1:1:1 volume mix of AAV_8-EFS-dSaCas9-KRAB-Dio, AAV_9-CamKII-0.4-
177 Cre-SV40 (Addgene, cat# 05558-AAV9) and AAV_5-U6-Cacna1eAC-EFS-GFP-KASH was
178 injected into the NAcLat. For a no gRNA control condition, 400 nL of a 1:1 volume mix of AAV_8-
179 EFS-dSaCas9-KRAB-Dio and AAV_9-CamKII-0.4-Cre-SV40 was infused into the NAcLat.
180

181 For mapping inputs to VTA cells in mice with *Cacna1e* downregulation in NAcLat, during a single
182 surgery, 300 nL of a of a 1:1 volume mix of AAV_5-FLEx^{loxP}-TC and AAV_5-FLEx^{loxP}-RABV-G was
183 injected into the VTA bilaterally, 600 nL of a 1:1:1 volume mix of AAV_8-EFS-dSaCas9-KRAB-Dio,
184 AAV_9-CamKII-0.4-Cre-SV40, and AAV_5-U6-Cacna1eAC-EFS-GFP-KASH was injected into the
185 left NAcLat, and 400 nL of a 1:1 volume mix of AAV_8-EFS-dSaCas9-KRAB-Dio and AAV_9-CamKII-
186 0.4-Cre-SV40 was injected into the right NAcLat. This study design enabled controls within the
187 same mice to prevent systematic biases due to differences in treatment of the mice. After 14 days,
188 RABVΔG was injected into the VTA. Mice were sacrificed five days later, and brains processed
189 as described below.
190
191 Brain section preparation, imaging, and cell counting: Five days after RABV injection, mice
192 underwent transcardial perfusion with 1x PBS followed by 4% formaldehyde in 1x PBS. Brains
193 were extracted and post-fixed in 4% formaldehyde for 24 hours, and then dehydrated with 30%
194 sucrose in 1x PBS. Brains were cut into 60 µm slices using a cryostat and mounted on Superfrost
195 Plus™ microscope slides (Fisher, cat # 1255015). Once the brain sections were fully dried on the
196 slide, they were rehydrated in 1xPBS containing DAPI at a dilution of 1:1000 (ThermoFisher, cat#
197 D1306). After 10 minutes, the liquid was removed, and Fluoromount-G (SouthernBiotech, cat#
198 0100-01) was applied to the sections. Coverslips (Thermo Scientific, cat# 152460) were used to
199 cover the brain sections on the slides. Images of the entire slides were captured using an Olympus
200 IX83 microscope, and manual cell counting was performed on the acquired images.
201
202 Determination of CRISPRi-mediated knockdown efficiency: To determine the efficacy of CRISPRi
203 knockdown of *Cacna1e* expression levels, 10 days following AAV injections into the NAcLat,
204 NAcLat brain tissue was dissected out from the brains of injected mice, and tissue was pooled (5
205 mice for *Cacna1e* gRNA and 3 mice for no gRNA control). Total RNA was extracted with TRIzol,
206 and 50 ng of total RNA was used for RT-qPCR using the Luna Universal One-Step RT-qPCR Kit
207 (New England Biolabs, cat# E3005L) following the manufacturer's
208 instructions. Phosphoglycerate Kinase 1 (PGK1) was used as the housekeeping gene for
209 normalization of *Cacna1e* mRNA levels.
210
211 **Dimensionality reduction of RABV input data**
212 For RABV input mapping experiments, quantified inputs cells were binned into 22 regions: Cortex
213 (anterior cortex), NAcMed, NAcLat, NAcCore, DStr, VP, PO, Septum, BNST, EAM, EP, GPe, PVH,

214 LHb, MHb, CeA, LH, ZI, DR, LDT, PBN, and DCN. Altogether, this dataset consists of the input
215 cell counts for these 22 regions across 118 mouse brains, with n=4 or 5 for each condition.
216
217 RABV input tracing data were reported as the percentage of total quantified labeled RABV inputs,
218 as reported previously[7,10]. These data were further scaled using Z-score normalization. Principal
219 Component Analysis (PCA) was then implemented on these normalized data using the scikit learn
220 library in Python with default parameters[30]. Weights for PCA models were visualized as heatmaps,
221 reflecting the contribution of each feature to each principal component. To test for differences
222 between groups visualized in PC space, we assessed the value for each brain for each PC and if
223 comparing 2 conditions, used an unpaired t-test, and if >2 conditions, a one-way ANOVA and if p
224 < 0.05, followed by pairwise t-tests with multiple comparisons corrections (Dunnett or Tukey, as
225 appropriate). Input values were the first 3 principal components, and significant differences
226 between conditions for each principal component (drugs versus controls, for example) were
227 denoted as having a p-value of less than 0.05. Results are reported where relevant in the text or
228 in **Table S2**.
229
230 Uniform Manifold Approximation and Projection (UMAP), implemented using the UMAP library in
231 Python, was used to generate alternative visualizations of the RABV input data[31]. To choose and
232 standardize our UMAP parameters across analyses, we investigated which methods placed
233 mouse brains of the same type and treatment close together most consistently. For the distance
234 metric parameter, the metrics we found to perform best were Euclidean and cosine, but we chose
235 to use the Euclidean metric for consistency with previous analyses[32]. For the number of neighbors
236 parameter, we chose a large number, ⅓ the size of each of our datasets, for a more global view
237 of the data. Other parameters were kept at the default values. To account for the stochasticity of
238 individual embeddings, we applied UMAP 20 times to each data set and found the results to be
239 very similar, as found in previous analyses[32]. The results were then presented as correlograms.
240 Clustered heatmaps and plots of these data were made using a combination of the Python
241 packages seaborn[33] and matplotlib[34]. The seaborn clustermap function was implemented with
242 default values, including Euclidean distance as the distance metric.
243
244 Each PCA and UMAP representation of data show each animal as a point, and each point is
245 colored by the relevant condition, either genotype or drug administered. To better visualize the
246 distribution of a given condition in PCA and UMAP space, we overlaid the points with ellipsoids.

Ellipsoids were centered at the average coordinate of a condition and stretched one standard deviation along the primary and secondary axes.

Brain Region Selection in the Allen Mouse Brain Atlas

To compare our data with connectivity data from the Allen Institute, we converted our 22 brain regions into regions or groups of regions defined by the Allen Atlas. This was necessary as our region annotations defined while doing cell counts of the RABV data were at times different from the Allen Mouse Brain Atlas-defined regions. 22 brain regions were used for RABV analyses, but these were reduced to 20 brain regions (NAcMed, NAcLat, and NAcCore were merged into the NAc) for comparison with Allen Atlas data. In several cases, multiple Allen-defined regions were used to constitute a single region that we defined, as in the case of the cortex. A summary of these conversions is as follows:

Full brain region name	Standard abbreviation	Allen abbreviations
Cortex	Anterior cortex	PL, ILA, ORB, GU, AI, MOs, MOp
Nucleus accumbens (medial)	NAcMed	ACB
Nucleus accumbens (lateral)	NAcLat	ACB
Nucleus accumbens (core)	NAcCore	ACB
Dorsal striatum	DStr	STRd
Ventral pallidum	VP	PALv
Preoptic area	PO	MPO, LPO
Septum	Septum	LSX, MS
Bed nucleus of the stria terminalis	BNST	BST
Extended amygdala area	EAM	MEA, AAA, NLOT, COA, MA, BMA, EPv, NDB
Internal globus pallidus	EP	GPi
External globus pallidus	GPe	GPe
Paraventricular nucleus of the hypothalamus	PVH	PVH
Lateral habenula	LHb	LH

Medial habenula	MHb	MH
Central nucleus of the amygdala	CeA	CEA
Lateral hypothalamus	LH	LHA
Zona incerta	ZI	ZI
Dorsal raphe nucleus	DR	DR, PAG
Laterodorsal tegmental nucleus	LDT	LDT
Parabrachial nucleus	PBN	PB
Deep cerebellar nuclei	DCN	CBN

It is important to note that these conversions are approximate, and brain-region specific results should be interpreted with caution, as there are known differences between atlases used in this work[35]. Representative images with boundaries showing every region on at least one section is shown in **Figure S1**.

Allen Mouse Brain Connectivity Atlas projection portrait construction

Projection portraits of the VTA were made using data from the Allen Mouse Brain Connectivity Atlas[36], as described previously[32]. Briefly, data from 20 input brain regions, as defined in the above table, were downloaded and used for analyses. Cre-based and non-Cre-based experiments representative of each brain region were chosen for visualization. Labeled cell bodies at the site of injection often spread into adjacent brain regions or only covered a part of a region. Several experiments were chosen to account for this variation and give a better estimate for each region's projections. Experiment IDs are recorded in **Table S1** and in our previous work[32]. Connectivity of brain regions of interest to the VTA was visualized by showing a representative slice of the VTA and coloring the image based on high or low connectivity according to averaged AAV tracing data. AAV tracing data were averaged across experiments and across brain regions that grouped together according to weights assigned by PCA, as shown in **Figures 2, 6, and 7**.

Data for projection portraits and for subsequent network construction was accessed using the python Allen SDK package, developed and maintained by the Allen Institute for Brain Science.

Gene Expression Data Access and Processing

Gene expression data was downloaded from the Allen Institute's Anatomic Gene Expression Atlas (AGEA)[37], an *in situ* hybridization dataset which has annotated expression of 19,932 genes to

every brain region defined in the Allen Mouse Brain Atlas. We used code written by Eli Cornblath (https://github.com/ejcorn/mouse_abi_tool) to access and download gene expression data for our regions of interest, as done in a previous study[38]. To ensure only high-quality data were included in our analyses, we filtered experiments based on metrics used in previous analyses of this dataset[39]. We retained genes for which there were data from coronal sections, or where the Pearson correlation coefficient across experiments was over 0.5 for a particular gene in our regions of interest. This filtering left us with 4,283 unique genes for the 36 Allen-defined brain regions to be aggregated to compare with our 22 quantified input sites from the RABV mapping data. We averaged data among brain regions that were defined differently in the atlas versus our RABV quantifications, which resulted in a total of 20 brain regions for comparative analyses, as detailed above. Data were normalized using a scaled sigmoid function, a method that is robust to outliers and was used in previous analyses of these data[40].

Gene expression data analysis and comparison to RABV data

To investigate how basal gene expression might be correlated to connectivity changes after drug exposure, we used processed data from the AGEA. For each experimental condition, the RABV data for the drug-treated animals were compared to those of the saline-treated controls. To quantify this comparison, we computed a ratio, as used in **Figures 9 and S10-S12**, by dividing the average RABV counts in each brain region for the experimental condition by the average RABV counts in each brain region for the saline condition. This resulted in a vector of 22 ratios for each experimental condition, one ratio for each brain region. We also computed a difference, as used in **Figures 8 and S7-S9**, by subtracting the average RABV counts in each brain region for the experimental condition by the average RABV counts in each brain region for the saline control condition. This resulted in a vector of 22 differences for each drug comparison, one difference for each brain region.

We calculated the correlation of the condition-control differences with gene expression data for each region. The Spearman correlation coefficient between the gene expression across regions and our RABV differences was used because the correlative relationship between these values cannot be assumed to be linear. A similar method was used in previous analyses[39]. A high positive correlation between a gene and an experimental condition ratio was interpreted as a greater likelihood of a brain region to exhibit RABV labeling changes after drug exposure if this gene is highly expressed before drug exposure. A negative correlation between a gene and an

experimental condition ratio was taken to mean this region would be more likely to exhibit RABV labeling changes after drug exposure if the gene expression level is low.

We performed GO analysis on the top 50 most highly correlated genes and on the top 50 most negatively correlated genes. GO analysis was performed using the EnrichR package[41]. Lists of genes with highly positive or negative correlations to our condition differences were compared to GO annotations using the coding language R. The 2021 version of two databases were queried: GO Biological Process and GO Molecular Function. GO enrichment analysis results were visualized in dot plots using the package ggplot2, as shown in **Figures 8 and S7-S9**. The 'overlap' term on the x-axis of these plots means the number of genes in the correlated gene lists that were also within the list of genes for the corresponding GO term.

We next compared the drug/isoflurane ratios for a group of addictive drugs to gene expression of subsets of genes of interest (**Figure 9, S10**). Similar analyses were done for ketamine/xylazine and fluoxetine (**Figure S11, S12**). The subgroups of genes used were synapse-related genes[42], ion-channel related gene[43], neurotransmitter receptor-related genes[44], differentially expressed genes related to substance dependence GWAS[45], and exo- and endocytosis-related genes[46]. Other subsets of genes of interest were defined using the Guide to Pharmacology database[47]. Correlation coefficients (Spearman's ρ) and p-values are reported in the figures.

RESULTS:

Dimensionality reduction methods identify differences in inputs of VTA cell populations

We and others previously showed that DAergic, GABAergic, and glutamatergic cells in the VTA receive inputs from similar brain regions, with some quantitative differences that varied depending on the study[10,12]. In our work we also showed that connectivity differences in the VTA are largely a consequence of spatial organization of cells within the VTA[7,10,32]. The fact that the distributions of these three VTA cell populations are largely spatially overlapping may explain why the global inputs to each population are similar. However, one limitation in interpreting these studies is that they focused on individual comparisons of input counts on a per region basis. While this is a common approach in analyzing viral tracing data, and useful for both hypothesis generation and testing, it fails to account for the higher-level organization of input patterns. Our goal here is to go beyond considering single brain regions and better understand the holistic connectivity patterns of different cell populations or drug treatment conditions.

350 Our first goal was to explore the potential differences in input patterns generated using RABV
351 tracing to each of the DAergic, GABAergic, and glutamatergic neuron populations in the VTA
352 using principal component analysis, PCA. A schematic of the experiment is shown in **Figure 1A**,
353 with representative images of brain regions of interest in **Figure 1B**. A standard representation of
354 these data, a bar plot, is shown in **Figure 1C**. PCA embedding resulted in the three cell
355 populations clustering into largely distinct groups (**Figure 1D**). We considered the first two
356 principal components (PCs), which explain the most variance in the data. In PC space, DAT-Cre
357 brains were characterized by low PC1 and low PC2 values, GAD2-Cre brains by high PC1 values,
358 and vGluT2-Cre brains by high PC2 values. The differences we noted were statistically significant:
359 PC1 values of GAD2-Cre compared to DAT-Cre brains were significantly different (One-way
360 ANOVA $p = 0.010$, DAT-Cre vs. GAD2-Cre multiple comparisons adjusted $p = 0.0087$; **Figure 1E**)
361 and PC2 values of DAT-Cre compared to vGluT2-Cre brains were significantly different (One-way
362 ANOVA $p = 0.016$, DAT-Cre vs. vGluT2-Cre multiple comparisons adjusted $p = 0.016$; **Figure 1F**).
363 An advantage of PCA over other dimensionality reduction approaches is that, because it is a
364 linear approach, the weights of each feature's contribution to each PC can be clearly interpreted.
365 In this case, we can infer which brain regions contribute most to the positive and negative
366 dimensions of each PC. For example, in our data, DAT-Cre and GAD2-Cre brains were separated
367 along PC1. Brain regions that contributed to the positive dimension of PC1 were the BNST,
368 entopeduncular nucleus (EP), GPe, central amygdala (CeA), and zona incerta (ZI) (**Figure 1G**).
369 These inputs were enriched onto GABAergic cells relative to DA cells (**Figure 1C**). To identify
370 where in the VTA these input populations projected, we assembled projection portraits of these
371 inputs to the VTA as we did previously[32]. This approach uses axonal projection data available
372 from the Allen Mouse Brain Connectivity Atlas to generate spatial heatmaps that show "hotspots"
373 of innervation in the midbrain[36]. We first selected experiments where GFP was expressed in the
374 input regions of interest. Pixel values representing projection density were pulled from a
375 representative coronal slice containing the VTA for each region. For a given set of inputs of
376 interest, we averaged together their projections to the VTA to see if the group had any common
377 spatial trends (**Figure 2A**). The projection portrait of the positive PC1 inputs indicated that they
378 preferentially project dorsally and laterally to areas surrounding the VTA (**Figure 2B**). In contrast,
379 the regions that contributed most strongly to the negative dimension of PC1 were the anterior
380 cortex, nucleus accumbens medial shell (NAcMed), ventral pallidum (VP), preoptic area (PO),
381 septum, lateral habenula (LHb), medial habenula (MHb), and lateral hypothalamus (LH). These
382 inputs were more highly labeled in DAT-Cre mice. The projection portrait of these inputs highlights
383 the whole VTA and not surrounding regions (**Figure 2C**). While the distribution of starter cells in

384 the VTA in DAT-Cre and GAD2-Cre mice is spatially overlapping[7], this analysis indicates that
385 inputs with biases onto DA cells target the VTA itself while those biased onto GABAergic cells
386 preferentially target areas dorsal and lateral to the VTA.
387
388 While DAT-Cre and GAD2-Cre conditions were separated along PC1, DAT-Cre and vGluT2-Cre
389 conditions were separated along PC2. Regions that contributed to the positive dimension of PC2
390 included the LHb, MHb, EP, ZI, and deep cerebellar nuclei (DCN) as well as the cortex, while
391 those contributing to the negative dimension included the NAcMed, nucleus accumbens lateral
392 shell (NAcLat), nucleus accumbens core (NAcCore), dorsal striatum (DStr), and GPe (**Figure 2D-**
393 **E**). The MHb and LHb both project medially in the VTA, whereas the NAcMed, NAcLat, NAcCore,
394 DStr, and GPe all project laterally[32]. The projection portrait corresponding to the positive
395 dimension of PC2 highlights the area dorsal of the VTA, as well as the medial aspect of the VTA
396 (**Figure 2D**), while those corresponding to the negative dimension highlight the ventrolateral
397 aspect of the ventral midbrain, including the substantia nigra pars reticulata (SNr) (**Figure 2E**).
398 These results are consistent with the medial-lateral projection gradient that principally divides the
399 projections into the VTA, with inputs from the basal ganglia projecting to the lateral portion of the
400 VTA and the habenula projecting to the medial portion[32]. As inputs from the MHb and LHb
401 contribute positive weights to the PC2 axis and vGluT2-Cre brains have the most positive PC2
402 values, it suggests that most of the vGluT2-expressing cells in the VTA are located within the
403 medial portion of the VTA. This is consistent with previous reports using immunohistochemistry
404 and in situ hybridization[48,49]. In addition, the EP, ZI, and DCN all project predominantly to the red
405 nucleus, and the cortex also innervates the red nucleus, which contains glutamatergic neurons
406 and is located dorsal to the VTA (**Figure 2D**). While injections for our viral mapping studies
407 targeted the VTA and most starter neurons were within the VTA, there were some starter neurons
408 in vGluT2-Cre brains located in the red nucleus. In contrast, this was not the case in DAT-Cre
409 brains[10]. As these starter populations were also largely spatially overlapping, the data indicate
410 that inputs with biases onto glutamatergic cells target the dorsomedial aspect of the VTA, while
411 those with a relative bias onto DA cells preferentially target the ventrolateral aspect of the VTA.
412
413 While PCA is particularly useful due to the interpretability of the weights of the PCs, it cannot
414 capture non-linear relationships in high-dimensional data, which are common in complex systems
415 like in neuroscience. To examine the overall relationship of input patterns between DAT-Cre,
416 GAD2-Cre, and vGluT2-Cre cell populations, we performed a second analysis on inputs from
417 each population using Uniform Manifold Approximation and Projection, UMAP, which can capture

418 more complex relationships than PCA. We found that DAT-Cre and GAD2-Cre brains were the
419 most separated in UMAP space, with vGluT2-Cre brains located between them (**Figure 2F**). This
420 is consistent with the overlap in neurotransmitters released by these cells: cells expressing DA
421 markers such as tyrosine hydroxylase (TH) and traditional GABAergic markers such as GAD2 are
422 nearly mutually exclusive, while there is considerable overlap between cells expressing DA
423 markers and glutamatergic markers, as well as cells expressing GABAergic markers and
424 glutamatergic markers[10,12,50–52]. Note that while DA neurons have been found to co-transmit DA
425 and GABA[53,54], this occurs through a non-canonical GABA synthesis pathway, and therefore DA
426 cells do not express typical markers of GABAergic cells, such as GAD2, used to define the Cre
427 line in our study.
428
429 Since individual UMAP embeddings are stochastic depending on initial seeding conditions, we
430 examined the average Euclidian distance between pairs of brains in 20 UMAP embeddings and
431 plotted the averaged results as a correlogram. This showed that DAT-Cre and vGluT2-Cre brains
432 were more like one another, and the GAD2-Cre brains were the most distinct from the other
433 conditions (**Figure 2G**). These results are thus consistent with the known neurochemical overlap
434 between these cells and indicate that DAT-Cre and vGluT2-Cre label more overlapping cells with
435 each other than with GAD2-Cre. In sum, these results serve to demonstrate that we can
436 recapitulate the locations of different neurochemically-defined cells in the VTA based on PCA and
437 projection portraits based on information from RABV input mapping data. They also provide a
438 validation of our approach for dissecting the relationships between input patterns and different
439 cell types within the VTA, as the conclusions about the relationship between input regions and
440 cell types agree with other studies using different, complementary methodologies.
441
442 **A single injection of an addictive drug changes brain-wide input patterns to VTA^{DA} cells**
443 With our dimensionality reduction approaches validated on our cell type-specific RABV data, we
444 next applied them to examining how addictive drugs may alter VTA input patterns. We first
445 assessed whether the psychoactive but non-addictive fluoxetine altered brain-wide input patterns
446 relative to saline-injected mice. We found no clear differences in inputs between these conditions,
447 and they overlapped completely in PC space – with no significant differences in PC1, PC2, or
448 PC3 between the saline and the fluoxetine brains ($p > 0.05$ for PC1-3) - indicating fluoxetine did
449 not alter brain-wide input patterns to VTA^{DA} cells (**Figure 3A-F**). We therefore combined these
450 groups for additional statistical power and tested whether a single administration of one of several
451 addictive drugs caused changes in brain-wide input patterns to VTA^{DA} cells, first considered as a

452 single group. When comparing combined controls to the drugs group, we observed a statistically
453 significant difference in input patterns, including a reduction in inputs from the DStr and elevation
454 in inputs from the GPe following drug injection (**Figure 3G**). In order to more fully assess which
455 input sites may differentiate the control- versus drug-treated groups, we again used PCA (**Figure**
456 **3H-I**). There was no significant difference between drugs and controls in PC1 ($p = 0.78$; **Figure**
457 **3J**). The differences in PC2 and PC3 were statistically significant: as we observed visually, the
458 control group's PC2 and PC3 values were significantly different from the drug group's PC2 and
459 PC3 values ($p = 0.0009$ and $p = 0.024$ for PC2 and PC3, respectively; **Figure 3K-L**). The positive
460 axis of PC2, which was enriched in drug-treated brains, was driven by inputs from EAM, EP, GPe,
461 LH, and PBN, while the negative axis was driven by the NAcMed, NAcCore, DStr, septum, and
462 MHb (**Figure 3M**). Notably, the most negative weights for PC2, namely the NAcMed, NAcCore,
463 DStr, septum, and MHb are all reduced in drug-treated brains (**Figure 3G**). Conversely, the most
464 positive weights, namely the EAM, EP, GPe, LH, and PBN, are all increased in drug-treated brains
465 (**Figure 3G**). Therefore, while PCA allows us to observe trends consistent with traditional methods,
466 we can also observe the relationship between the percentage of inputs among different brains,
467 and also identify relationships that are not immediately apparent in the data when presented as
468 bar graphs. For example, while the BNST, CeA, and ZI do not show clear differences in control
469 vs. drug-treated brains in the bar graphs, they are all positive weights in PC2 and thus, likely
470 change in concert with regions such as the GPe and PBN (**Figure 3G-M**).
471
472 Importantly, unlike traditional bar graph approaches, PCA allows us to isolate technical variation
473 from the experiments, enabling us to focus more clearly on changes induced by the relevant
474 variable, here treatment with a control substance or addictive drug. For example, PC1 does not
475 distinguish control vs. drug-treated brains (**Figure 3H, J**), indicating this variable was inherent to
476 the way the experiment was performed and not related to drug or control treatment. The strongest
477 negative weights for PC1 were the NAcLat, NAcCore, DStr, and GPe, while the strongest positive
478 weights for PC1 were the VP, PO, LHb, and DR (**Figure 3M**). This is consistent with connectivity
479 differences along the medial-lateral axis of the VTA, which underlies many of the connectivity
480 differences to different VTA^{DA} subpopulations[7,10,32]. To assess whether PC1 may reflect
481 differences the location of starter cells in the VTA, we first assessed whether there was a
482 systematic difference in starter cell location between conditions. We noted a high level of overlap
483 in starter cell distribution between conditions (**Figure 4A, S2**), indicating that this alone likely did
484 not explain differences between control and drug-treated groups. We then assessed whether
485 brain to brain variation in starter cell distribution could explain the effects observed along PC1.

486 We therefore colored each point in PC space according to the assessed center of injection for
487 each experiment. We noted a clear medial-lateral gradient along PC1, but not PC2 or PC3 (**Figure**
488 **4B-C**). To test the significance of this relationship, we performed linear regression analysis,
489 comparing the x-coordinate of the injection center relative to location along PC1, PC2, or PC3 for
490 each brain. We observed a highly significant positive correlation with PC1, a slightly positive but
491 non-significant correlation with PC2, and no correlation for PC3 (**Figure 4D-F**). These results
492 show that PC1 reflects variation in the injection site within the VTA, while PC2 reflects changes
493 induced by addictive drugs, allowing us to isolate the changes in input connectivity induced by
494 administration of a single addictive drug.
495
496 With our integrative methodology validated on cell type-specific RABV data and demonstrating
497 that addictive drugs alter brain-wide input patterns to VTA^{DA} cells, we applied our approaches to
498 explore the effects of each drug specifically, as well as potential effects of the 2x use of the K/X
499 anesthetic mixture. We first asked two questions: 1) How do injections of different addictive drugs
500 change the connectivity patterns onto VTA cells? 2) How do these potential drug-induced
501 differences relate to differences between unique cell types in the VTA? To answer these, we first
502 assessed experiments with ten separate experimental conditions: 2 conditions of GAD2-Cre mice,
503 and 8 conditions of DAT-Cre mice. The GAD2-Cre mice were all anesthetized with isoflurane and
504 administered either saline or cocaine one day prior to RABV injection. The DAT-Cre mice were
505 given either isoflurane or K/X-based anesthesia. The K/X-anesthetized mice were administered
506 saline. The isoflurane-anesthetized mice were administered either saline, fluoxetine,
507 amphetamine, cocaine, methamphetamine, morphine, or nicotine. RABV mapping was performed
508 from targeted VTA cells in all cases, and the brain-wide inputs were quantified. We then performed
509 PCA on the combined RABV tracing datasets, which showed that brains from GAD2-Cre mice
510 were in the positive dimension of PC1, while those from DAT-Cre mice were in the negative
511 dimension (**Figure 5A**), regardless of the substance administered. This difference in PC1 was
512 highly statistically significant (One-way ANOVA $p < 0.0001$; all conditions pairwise comparisons
513 with GAD2-Cre, multiple comparisons adjusted $p < 0.0001$; **Figure 5B**). The positive dimension
514 of PC1 received contributions from largely the same sets of regions as in the previous analysis of
515 DAT-Cre, GAD2-Cre, and vGluT2-Cre brains, which included the BNST, EP, ZI, CeA, as well as
516 the DCN (**Figure 5C, 1G**). Given that the same set of brain regions differentiated DAT-Cre and
517 GAD2-Cre brains along PC1 in both datasets, this suggests that the intrinsic differences in inputs
518 to different cell populations in the VTA are more pronounced than differences induced by addictive
519 drugs, fluoxetine, or the method of anesthesia. Notably, these patterns were unlikely to be

obtained by chance; scrambling the sample identity and percentage of RABV-labeled cells in each input site resulted in groups that overlapped in both PCA and UMAP space (**Figure S3**).

To specifically explore potential drug-induced differences in input labeling onto VTA^{DA} cells, we removed GAD2-Cre brains from the dataset. Results and representative images are shown in **Figure 5D-E**. In PCA analyses of these brains only, PC1 and PC3 largely failed to differentiate the conditions, with no significant differences observed, while PC2 significantly differentiated the conditions (One-way ANOVA $p = 0.0093$; saline vs. drugs multiple comparisons adjusted $p = 0.034$; **Figure 5F-J**). The most negative weights to PC1 were contributed by the basal ganglia inputs (**Figure 5K**) that project to the SNr, located ventrolaterally to the VTA (**Figure 6A**) while positive contributors came from brain regions that projected more medially (LHb, MHb, dorsal raphe (DR)) and centrally to the VTA (ventral pallidum (VP), PO, extended amygdala area (EAM), paraventricular nucleus of the hypothalamus (PVH), and LH) (**Figure 5K, 6B**). This is consistent with a gradient along the medial-lateral axis[32]. As it did not differentiate the conditions, this axis likely represents experimental variations in the location of starter cell populations within the VTA[7,10,32]. The regions with the largest positive contribution to PC2 included the EAM, parabrachial nucleus (PBN), DR, EP, and LH, with lesser contributions from the GPe, DCN, ZI, CeA, and BNST (**Figure 5K, 6C**). These regions were over-represented in animals treated with a single administration of an addictive drug. Notably, this group of inputs contained brain regions that are involved in the brain's stress response such as the PBN, EAM, CeA, and BNST, and have been implicated in drug-induced behaviors[55,56]. For example, we recently showed the importance of the GPe in conditioned place preference and locomotor sensitization and the BNST in drug-induced withdrawal[15,25]. The regions with the largest negative contribution to PC2 included the NAcMed, NAcCore, DStr, Septum, and MHb (**Figure 5K, 6D**). These regions were underrepresented in animals given a single administration of an addictive drug. These results together demonstrate that addicive drugs cause long-lasting changes in input populations to DA cells, and that we can identify which sets of inputs distinguish drug-treated vs. control-treated brains. These changes may be functionally important, as we previously demonstrated the functional role of two inputs, the GPe and BNST, that we identified as differing between drug-treated and control conditions[25,57].

Lastly, we wanted to explore the overall relationship between input changes induced by different drugs. As before, we used UMAP to explore the higher-level organization of these conditions to compare the relationship of holistic input patterns between groups. We found that the mice

554 anesthetized with isoflurane and treated with saline overlapped with the isoflurane-anesthetized,
555 fluoxetine-treated group and the K/X-anesthetized and saline-treated group, but segregated from
556 animals treated with the addictive drugs - psychostimulants, morphine, and nicotine (**Figure 6E**).
557 Our analysis of the relationships between individual conditions, generated using the Euclidian
558 distances between points in 20 UMAP embeddings as before, demonstrated that the expected
559 control conditions formed a cluster (saline, fluoxetine) distinct from the other groups. Interestingly,
560 the K/X-anesthetized animals were more closely associated with the mice treated with addictive
561 drugs, in particular morphine, than with controls (**Figure 6F**). This suggests that addictive drugs
562 cause similar changes in brain-wide input patterns to one another in DAT-Cre mice, and that input
563 patterns in K/X-anesthetized animals more closely resemble morphine-treated mice than saline-
564 treated mice. This indicates that the method of anesthesia, either using isoflurane or K/X, results
565 in different patterns of input labeling. Given the similarity of input patterns in K/X-anesthetized
566 mice to isoflurane-anesthetized mice treated with an addictive drug but not saline, we suspect
567 that two doses of K/X-anesthesia as is required for RABV circuit mapping experiments triggers
568 changes in input patterns in rodent brains that last at least the five-day duration of these
569 experiments.
570
571 **Anesthetic doses of K/X cause long-lasting changes in inputs to VTA^{DA}→NAcLat and**
572 **VTA^{DA}→Amygdala cells**
573 To examine how differences in anesthesia methods may impact brain-wide input patterns, we
574 performed some more targeted comparisons. When comparing only two groups using PCA –
575 isoflurane-anesthetized animals to K/X-anesthetized animals – these conditions completely
576 segregated (**Figure 7A**). While the difference in PC1 was not quite significant ($p = 0.086$), the
577 difference in PC2 was significant ($p = 0.037$). This separation was driven by positive weights from
578 the VP, PO, EAM, PVH, LH, and PBN along PC1, which were more strongly represented in the
579 K/X-anesthetized mice and whose combined projection portrait broadly targets the VTA (**Figure**
580 **7A-D**), and the NAcLat, DStr, GPe, and PVH along PC2, which were also more strongly
581 represented in the K/X-anesthetized mice whose combined projection portrait targets
582 ventrolateral to the VTA (**Figure 7A-C, E**). A similar separation of conditions was observed using
583 UMAP (**Figure 7F**).
584
585 Next, we wanted to assess which VTA^{DA} cells may be impacted by whether the animals received
586 isoflurane or K/X-based anesthesia. To test this, we performed cell type-specific Tracing of the
587 Relationship between Inputs and Outputs (cTRIO) for each of four different VTA^{DA} subpopulations:

588 those projecting to the NAcMed, NAcLat, Amygdala, or mPFC, and receiving K/X anesthesia and
589 saline, isoflurane and saline, or isoflurane and cocaine. The differences in input patterns between
590 conditions were most pronounced for VTA^{DA}→NAcLat cells, where the isoflurane- and K/X-treated
591 groups segregated (**Figure 7G-H**). Groups appeared to differ along both PC1 and PC2, though
592 differences in PC2 were not statistically significantly different. K/X-treated brains were
593 characterized by lower PC1 values which received contributions principally from the anterior
594 cortex, NAcMed, NAcLat, NAcCore, septum, PVH, and MHb, as well as higher PC2 values which
595 received contributions from the VP, PO, EAM, LHb, and LH (PC1, One-way ANOVA $p = 0.0003$,
596 saline vs. cocaine multiple comparisons adjusted $p = 0.011$, K/X vs. cocaine multiple comparisons
597 adjusted $p = 0.0002$; **Figure 7G, I-K**). The following comparisons in PC1 were statistically
598 significant: cocaine versus isoflurane controls ($p = 0.011$) and cocaine versus K/X anesthesia (p
599 $= 0.001$) (**Figure 7G**). Notably, K/X, saline-treated mice and isoflurane, cocaine-treated mice
600 segregate from one another in PCA space, indicating that the K/X-induced changes are distinct
601 from those induced by cocaine (**Figure 7G-I**). The similarity in projection portraits for weights that
602 contribute more to the K/X-treated group in VTA^{DA}→NAcLat (**Figure 7J-K**) and all VTA^{DA} neurons
603 (**Figure 7D-E**) suggests that largely overlapping DA cells may be targeted for each set of
604 experiments and is consistent with the observation that VTA^{DA}→NAcLat neurons comprise the
605 majority of VTA^{DA} neurons, as noted in previous studies[7,10]. As with all VTA^{DA} cells, similar results
606 were observed for VTA^{DA}→NAcLat cells in both in PCA and UMAP space (**Figure 7L**). These
607 results thus serve as another proof of principle of the reliability of our approach to pull out similar
608 results from different datasets.
609
610 In addition to VTA^{DA}→NAcLat cells, we observed some segregation of isoflurane and K/X-treated
611 conditions in VTA^{DA}→Amygdala cells (**Figure 7M-P**). The lack of clear differentiation in PCA
612 space, with only PC3 showing significant differences between the isoflurane control group and
613 K/X anesthesia (One-way ANOVA $p = 0.014$, saline vs. K/X multiple comparisons adjusted $p =$
614 0.0078; **Figure S4**) makes it difficult to interpret which input sites may be contributing to the
615 differentiation in conditions that we observed. In the VTA^{DA}→NAcMed and VTA^{DA}→mPFC
616 subpopulations, the separation between isoflurane-saline, isoflurane-cocaine, and K/X-saline
617 conditions was much less pronounced (**Figure S5**), and not significant; indeed, similar
618 separations were observed by chance (**Figure S6**). Notably, when considering inputs to all VTA^{DA}
619 cells, the projection portraits that indicate the inputs most highly elevated or depressed in K/X-
620 treated mice highlight either the entire VTA, or the ventrolateral aspect of the VTA (**Figure 7D-E**).

621 These projections are consistent with the locations of the VTA^{DA}→Amygdala and VTA^{DA}→NAcLat
622 cells, respectively, within the VTA. In contrast, the portraits do not highlight the medial or
623 ventromedial aspects of the VTA, which is the location of VTA^{DA}→mPFC and VTA^{DA}→NAcMed
624 cells[32,58]. These results together indicate that K/X anesthesia impacts inputs that preferentially
625 target VTA^{DA}→NAcLat or VTA^{DA}→Amygdala cells.
626
627 **Exploring gene expression patterns that predict changes in RABV input labeling**
628 We next wanted to explore if drug-induced changes in input connectivity might be related to gene
629 expression profiles in cells located in the input sites. To do this, we calculated the correlation of
630 gene expression data from the Allen Gene Expression Atlas (AGEA) with the difference (**Figure**
631 **8**) between RABV-labeled inputs labeled in each region in experimental conditions and
632 isoflurane/saline-treated controls. Notably, the AGEA data are from all cells in the input regions
633 and are not limited to those projecting to the VTA and show only baseline gene expression
634 patterns and not those following drug administration. Nonetheless, these analyses can be a
635 valuable starting point in associating spatial gene expression data with patterns of RABV-labeled
636 inputs from VTA^{DA} cells. After filtering AGEA data for only high-quality experiments, we were left
637 with 4,283 genes to which we could calculate correlations within our 22 input brain regions of
638 interest.
639
640 We first identified genes or pathways that may be linked to elevations or depressions in RABV
641 labeling for each condition. We selected genes that were highly positively or negatively correlated
642 to differences between 1) isoflurane-saline controls and 2) isoflurane- psychostimulant, morphine,
643 nicotine, or fluoxetine, or 3) K/X-saline mice. We used the top 50 genes in the AGEA data that
644 were either positively or negatively correlated (Spearman's ρ) to differences in RABV labelling
645 and performed gene ontology (GO) analyses. Starting with addictive drugs in aggregate, the 50
646 most positively correlated genes (Spearman's $\rho > 0.47$, $p < 0.05$) were most significantly
647 associated with inhibitory ligand-gated chloride channels (**Figure 8A**), suggesting that higher
648 basal expression of these genes may be related to larger changes in connectivity induced by a
649 single dose of an addictive drug. Conversely, there were many more genes that were strongly
650 negatively correlated to drug-induced changes in RABV labeling. The 50 most negatively
651 correlated genes (Spearman's $\rho < -0.68$, $p < 0.001$) were most closely associated with negative
652 regulation of long-term synaptic potentiation (**Figure 8B**), suggesting that regulation of synaptic
653 plasticity in input cell populations may be a key indicator of the likelihood of an addictive drug
654 altering RABV input labeling. We repeated this analysis of the top 50 genes with each individual

655 drug: cocaine, methamphetamine, amphetamine, morphine, and nicotine. In addition to findings
656 in aggregate, other interesting classes of genes that were negatively associated (Spearman's ρ
657 < -0.50, $p < 0.05$) with individual drug-induced changes in RABV labeling include regulation of
658 synapse structural plasticity (methamphetamine), regulation of calcium (Ca^{2+}) ion transport
659 (nicotine), cellular response to Ca^{2+} ions (cocaine), and regulation of potassium ion transporters
660 (nicotine) (**Figure S7**), which relate to synaptic and cellular processes of plasticity and intrinsic
661 excitability. There were fewer than 50 genes that were significantly positively correlated, but the
662 top 50 genes (Spearman's $\rho > 0.36$, $p < 0.12$) were associated with terms including anion
663 channels (cocaine, amphetamine, methamphetamine) and syntaxin binding (cocaine,
664 amphetamine, nicotine) (**Figure S8**). We also explored which gene expression patterns may be
665 related to input changes driven by K/X anesthesia. Anion channel activity, particularly GABA
666 receptor expression, again shows up as one of the most significant associations to the top 50
667 most positively correlated genes (Spearman's $\rho > 0.37$, $p < 0.10$) (**Figure 8C**), while negatively
668 correlated genes were associated with a variety of metabolic processes (**Figure 8D**). Notably,
669 these gene expression patterns were not correlated with input changes induced by fluoxetine
670 (**Figure S9**).
671
672 To further assess which classes of genes were the most closely related to the differences in drug-
673 evoked RABV labeling relative to controls, we performed linear regressions of the ratios of RABV
674 labeling in experimental vs. control conditions relative to the mean of the log normalized
675 expression of AGEA RNA *in situ* hybridization data for a particular class of genes. We observed
676 an overall significant and slightly negative correlation between the RABV labeling ratio and the
677 gene expression mean ($r = -0.30$, $p = 2.1 \times 10^{-3}$) for all 4,283 genes (**Figure S10A**). This genome-
678 wide negative correlation is a useful reference to compare to correlation coefficients of subsets of
679 genes. Among the gene expression classes that we examined, the most significant association
680 was between the change in RABV-labeled inputs and ion channel gene expression ($r = -0.56$, p
681 $= 1.3 \times 10^{-9}$; **Figure 9A**), consistent with our results from GO analyses. The next most significant
682 classes were neurotransmitter receptors ($r = -0.46$, $p = 1.9 \times 10^{-6}$) and synapses ($r = -0.42$, $p =$
683 1.6×10^{-5}), followed by genes that have been linked to SUDs through Genome-Wide Association
684 Studies (GWAS; $r = -0.33$, $p = 7.7 \times 10^{-4}$) as well as endo/exocytosis genes ($r = -0.30$, $p = 2.3 \times$
685 10^{-3}). Each of the above relationships showed a negative correlation of RABV ratios with gene
686 expression (**Figure 9B-C, S10B-C**). Except for endo/exocytosis genes, each class had a more
687 negative, significant correlation than our genome-wide reference. As a further comparison, we
688 observed that the relationships between RABV labeling ratios and gene classes that are likely

689 irrelevant to RABV labeling, such as mitochondrial genes ($r = -0.24$, $p = 1.4 \times 10^{-2}$), sugar
690 transporters ($r = -0.26$, $p = 1.0 \times 10^{-2}$), and tumor-associated genes ($r = -0.18$, $p = 7.0 \times 10^{-2}$) were
691 weaker and less significant than our classes of interest (**Figure S10D-F**).
692
693 As the class of ion channel genes was the most strongly correlated to drug-induced differences
694 in RABV-labeled input patterns, we assessed which ion channels are most closely linked to RABV
695 labeling differences between conditions. The most significant relationship was between Ca^{2+}
696 channel genes ($r = -0.57$, $p = 4.4 \times 10^{-10}$), followed by Cl^- ($r = -0.39$, $p = 6.1 \times 10^{-5}$), K^+ ($r = -0.30$,
697 $p = 2.9 \times 10^{-3}$), and Na^+ channels ($r = -0.11$, $p = 0.30$; **Figure 9D-G**). The expression levels of
698 these channels, in particular Ca^{2+} channels, are linked to regulating a variety of cellular processes,
699 including immediate early gene expression networks as well as cellular excitability. Ligand-gated
700 channels ($r = -0.40$, $p = 4.1 \times 10^{-5}$) were more strongly related with RABV labeling than voltage-
701 gated ion channels ($r = -0.33$, $p = 7.4 \times 10^{-4}$) or other types of ion channels ($r = -0.13$, $p = 0.21$;
702 **Figure S10G-I**). Among the ligand-gated channels, the glutamate receptors were the most
703 strongly correlated ($r = -0.49$, $p = 3.1 \times 10^{-7}$; **Figure 9H**). The next most strongly correlated gene
704 classes were acetylcholine receptors ($r = -0.36$, $p = 2.4 \times 10^{-4}$), GABA receptors ($r = -0.31$, $p =$
705 1.8×10^{-3}), and glycine receptors ($r = 0.32$, $p = 1.4 \times 10^{-3}$) (**Figure 9I-K**). Notably, glycine receptors
706 were the only class of genes that we analyzed that was positively correlated with RABV labeling.
707 Similar patterns were observed for K/X anesthetized mice (**Figure S11**), but not with isoflurane-
708 anesthetized, fluoxetine-treated mice (**Figure S12**). These results together indicate that the basal
709 expression levels of a variety of ion channels, particularly Ca^{2+} and ligand-gated ion channels,
710 may be related to driving elevations or depressions in RABV labeling following a single injection
711 of a variety of addictive drugs, or K/X anesthesia.
712
713 **Functional validation of link between gene expression and RABV labeling**
714 As the correlation between RABV labeling ratios and Ca^{2+} channel gene expression was negative,
715 lower expression of Ca^{2+} genes was linked to an elevation in drug-induced RABV input labeling.
716 This relationship could be explained by several mechanisms. One, expression of Ca^{2+} channel
717 genes could be inhibitory towards the drug-induced change in RABV transmission. Alternatively,
718 lower Ca^{2+} channel gene expression levels could indicate more potential for a drug-induced rise
719 in gene expression level. To start differentiating between these possibilities, we performed
720 CRISPR-based gene expression modulation of the voltage-gated calcium ion channel *Cacna1e*
721 using CRISPRi, which reduces gene expression through blocking DNA transcription without
722 cutting DNA[59] (**Figure 10A-B**). *Cacna1e* was chosen as a test gene because it was one of the

723 Ca^{2+} channel genes included in **Figure 9D** that had a strong negative correlation with RABV
724 labeling, and was strongly expressed in the nucleus accumbens[37] (**Figure S13**). Three different
725 adeno-associated viruses (AAV) were co-injected into the NAcLat, an input site to the VTA, in
726 DAT-Cre mice. These viruses expressed 1) Cre, 2) Cre-dependent dCas9, 3) a Cre-dependent
727 small guide RNA (gRNA) targeting *Cacna1e*. A two AAV mixture lacking the AAV expressing the
728 gRNA was used as a control. The three AAV experimental mix was administered into the NAcLat
729 in one hemisphere, while the two AAV control mix was injected into the other hemisphere. During
730 the same surgery, AAVs expressing Cre-dependent TVA-mCherry and RABV glycoprotein were
731 bilaterally injected into the VTA, so that RABV mapping could be done in both hemispheres
732 (**Figure 10C-D**). Because the NAcLat, NAcCore, and GPe unilaterally project to the VTA in the
733 same hemisphere, and not the contralateral VTA[7,10,15,25], the ratio of labeled inputs in these sites
734 on a single hemisphere can be used to assess the relative labeling in the NAcLat in experimental
735 and control conditions within each mouse.
736
737 We first validated that our CRISPRi strategy reduced *Cacna1e* gene expression. We designed
738 our gRNA to cause only a mild reduction in *Cacna1e* expression to more naturally mimic potential
739 changes in gene expression. We found that our CRISPRi perturbation reduced gene expression
740 by ~20% (**Figure 10E**). This knockdown of *Cacna1e* in the NAcLat via CRISPRi resulted in
741 decreased RABV-labeled inputs from the NAcLat compared to controls where the gRNA was not
742 included (**Figure 10F**). These results indicate that reduced levels of *Cacna1e* likely lower the
743 number of RABV-labeled inputs from the NAcLat, and directly link the levels of *Cacna1e* and
744 RABV input labeling.
745
746 **DISCUSSION:**
747 Here we explored the long-term consequences of a single injection of a variety of addictive drugs
748 on the connectivity of VTA^{DA} cells. We first confirmed that dimensionality reduction approaches
749 could adequately differentiate the connectivity between different cell populations in the VTA, and
750 showed which inputs differentiate DAergic, GABAergic, and glutamatergic cells in the VTA
751 (**Figures 1-2**). We then showed that a variety of addictive drugs as well as K/X-based anesthesia
752 trigger long-lasting changes in the brain-wide input patterns to VTA cells, which were clearly
753 observable though less substantial than the differences onto different cell types or natural
754 variation in starter cell location (**Figures 3-6**). We used our cTRIO method to identify DA cell type-
755 specific changes induced by cocaine as well as K/X anesthesia, implicating the VTA^{DA}→NAcLat
756 and VTA^{DA}→Amygdala cells as those exhibiting the most substantial input changes (**Figure 7**).

757 We then explored intrinsic gene expression patterns throughout the brain that relate to the
758 elevation or depression in RABV labeling by different drugs, finding that expression levels of ion
759 channels, neurotransmitter receptors, and synapse-related genes were all significantly negatively
760 correlated with RABV input labeling ratios, with Ca^{2+} channels and glutamate receptors being the
761 most strongly correlated (**Figures 8-9**). We then demonstrated the causative role of one calcium
762 channel gene, *Cacna1e*, in influencing RABV input mapping efficiency (**Figure 10**).
763

764 **Addictive drugs induce changes in connectivity onto VTA^{DA} neurons from common and**
765 **distributed input populations throughout the brain**

766 Using dimensionality reduction approaches we differentiated the input patterns to different VTA
767 cells (**Figures 1-2**) and showed that these differences were larger than the differences in inputs
768 from the same cell populations in animals given an addictive drug vs. saline (**Figure 5A**). Notably,
769 these differences were unique from those triggered by the psychoactive but non-addictive
770 substances fluoxetine and K/X (**Figure 5**). Differences were apparent on the 2nd PC axis, which
771 were driven by positive weights from the GPe, EP, EAM, LH, ZI, DR, and PBN, regions that
772 showed elevated connectivity in drug-treated mice. Many of these regions have been implicated
773 in cocaine addiction[60–63]. While these drug-induced differences in input labeling were less
774 substantial than intrinsic cell type connectivity differences (**Figure 5A**) or differences in starter cell
775 location (**Figure 4**), these differences were more apparent when using dimensionality reduction
776 methods such as PCA and UMAP. That different cell types exhibit larger differences in input
777 patterns than the same cell type with and without drug administration is perhaps not surprising,
778 as different populations of cells may receive different sets of inputs from one another, and these
779 are likely more stable across experiments than the differences in connectivity triggered following
780 a single exposure to an addictive drug. The same is likely true for spatial gradients, which we
781 determined to be a major source of variation in RABV inputs to the VTA[32]. Notably, the minor
782 differences in starter cell location are likely not a technical concern specific to our study, but rather
783 inherent to all RABV mapping experiments that rely on intracranial injections, as a small amount
784 of biological or technical variation is to be expected. The PCA approach we employ here, however,
785 can better isolate these effects than traditional bar graph approaches and thus enable clearer
786 observation of the effect of the relevant variable being tested, here effects of a single drug
787 administration (or K/X anesthesia) on the input connectivity to VTA^{DA} cells. Importantly, these
788 analyses may provide important insight into the circuit mechanisms underlying SUDs; for example,
789 the GPe, LH, and PBN show up as high on PC2 from brains of mice treated with an addictive drug
790 (**Figure 5K**). We showed the importance of the GPe in behaviors elicited by cocaine[15,57], the

791 importance of the LH, in particular neuropeptides such as orexin, melanin-concentrating hormone
792 in reward learning and memory is well-known[64–67], and the PBN, while much less studied in the
793 context of addiction, is involved in regulating negative emotions, pain, and aversion, and has
794 begun to be implicated in SUD-related behaviors[68,69]. Thus, our data could be used to generate
795 new hypotheses about connections that are yet-unstudied but play important roles in addiction.
796
797 The results in this study further confirm our previous observations that a single exposure to a
798 variety of addictive drugs triggers long-lasting changes in inputs to VTA^{DA} neurons. Our
799 interpretation of these data is that the changes are largely being driven by a change in the activity
800 of input cells, as we have shown using fiber photometry and slice electrophysiology in three
801 separate studies[15,16,70]. However, we have not confirmed this to be true for all cases. As a single
802 exposure to a variety of addictive drugs alters the strength of both excitatory and inhibitory inputs
803 in the VTA[5,20–22], we cannot rule out that changes in synapse number or strength may also
804 influence the observed connectivity results.
805
806 **Ketamine/xylazine anesthesia alters the input landscape of VTA^{DA} cells**
807 Animals anesthetized with a K/X mixture showed a different pattern of input labeling to VTA^{DA}
808 cells than animals anesthetized with isoflurane (**Figure 7A-B**). While we cannot perform RABV
809 mapping on unanesthetized mice, making it impossible to definitively define which mode of
810 anesthesia, or both, alters RABV input patterns we suspect that isoflurane anesthesia has minimal
811 effect on the brain-wide inputs to VTA^{DA} cells. This is largely because animals treated with an
812 addictive drug with isoflurane anesthesia look more like those receiving K/X-saline than
813 isoflurane-saline animals (**Figures 5-6**). In addition, ketamine is a drug with known addictive
814 liability[71–74]. While the anesthetic doses used here (100 mg/kg) are well above the doses used
815 recreationally (~1 mg/kg), the changes that we observed with K/X anesthesia may be related to
816 the addictive liability of ketamine. Interestingly, the K/X-induced input changes were most similar
817 to those induced by 10 mg/kg of morphine (**Figure 6F**). Antidepressant doses of ketamine may
818 work in part via the opioid system; indeed, it has been known for some time that ketamine binds
819 to the mu opioid receptor[75–78], and it was more recently shown that the opioid antagonist
820 naltrexone blocks the antidepressant effects of ketamine[79,80]. Given that anesthetic doses of
821 ketamine (100 mg/kg) are roughly 10 times higher than antidepressant doses of ketamine (~10
822 mg/kg), K/X anesthesia almost certainly engages the opioid system.
823
824 **Relationship of gene expression with the extent of drug-induced RABV input labeling**

825 Gene expression patterns in the mouse brain are correlated with the extent of elevations and
826 depressions of RABV labeling induced by one of several addictive drugs. We observed a slightly
827 negative correlation of RABV labeling changes with the overall level of gene expression across
828 the brain. We are not sure of the implications of this negative correlation, though it could suggest
829 that if initial gene expression levels are lower, it leaves a higher potential for experience-induced
830 elevations. We observed significant negative correlations of RABV labeling changes induced by
831 addictive drugs with the levels of expression of ion channel genes, neurotransmitter receptor-
832 related genes, and synapse-related genes. These results and our experiments demonstrating the
833 functional impact of downregulating *Cacna1e* for RABV input labeling (**Figure 10**) indicate that
834 the expression levels of these genes could be used as predictive biomarkers of which regions are
835 likely to undergo drug-induced changes in connectivity to VTA^{DA} cells. They also suggest that the
836 expression levels of these gene classes are related to the drug-induced changes in RABV labeling.
837
838 While the AGEA is a useful resource for relating spatial gene expression information to our RABV
839 mapping datasets, there are notable limitations. First, the AGEA dataset is not as quantitatively
840 rigorous as modern single nucleus RNA sequencing or spatial transcriptomic datasets.
841 Nonetheless, we believe that the overall patterns of high and low expression, especially when
842 considered among classes of genes as was performed here, can still be informative. Furthermore,
843 the AGEA dataset provides a static picture of gene expression levels throughout the brain, and
844 thus does not account for potential changes in gene expression levels triggered by administration
845 of one of the drugs used in this study. Third, the AGEA dataset considers expression levels in all
846 cell types in a brain region, irrespective of their individual transcriptomic/molecular identities, while
847 only a subset of cells in a region project to VTA^{DA} cells. Nonetheless, our CRISPRi experiment
848 showing that a mild reduction of *Cacna1e* reduces RABV labeling indicates the potential for
849 causative associations between gene expression patterns and drug-induced RABV input labeling
850 changes (**Figure 10**). This result also directly links cellular excitability and the extent to which
851 RABV labels these cells as monosynaptic inputs to defined cell populations. While our
852 experiments do not prove that any particular gene expression changes drive changes in RABV
853 labeling, they provide a nice starting point for follow-up experiments.
854
855 Our RABV screen identified several input sites that show elevated or depressed labeling following
856 a single administration of an addictive drug, suggesting potential changes in excitability of these
857 cells. Ca^{2+} channel genes were also highly negatively correlated with the extent of drug-induced
858 changes in RABV input labeling. Ca^{2+} channels have been implicated in substance misuse

through Genome-Wide Association Studies[81], and molecules that target these channels have shown some promise as addiction therapeutics[82–87]. It is of particular interest that Ca^{2+} and not Cl^{-}, Na^{+}, or K^{+} channels are highly correlated to RABV input labeling changes. Ca^{2+} is critically involved as a secondary messenger in neurons that affects a variety of processes including long-lasting changes in transcription and synaptic transmission, whereas the other ions are mostly involved only in facilitating or inhibiting formation and propagation of the action potential. Understanding how Ca^{2+} channel gene expression levels relate to drug-induced changes in the brain will help to illuminate the relationship between basal gene expression levels, drug-induced changes in RABV labeling, and substance misuse, providing mechanistic insights into how inter-individual differences influence susceptibility to substance misuse.

ACKNOWLEDGEMENTS:
We would like to thank Hemmings Wu and Zhoule Zhu for their thoughtful critique of our manuscript.

AUTHOR CONTRIBUTIONS: KTB performed the majority of experiments, KB assisted with performing computational analyses of the data, PD assisted with network constructions and projection portraits, MH assisted with figure preparation, GT, JJV, and GA performed CRISPRi experiments, and KTB wrote the manuscript.

FUNDING: This work was supported by the NIH (R00 DA041445, DP2 AG067666, R01 DA054374, R01 DA056599, R01 NS130044), Tobacco Related Disease Research Program (T31KT1437, T31P1426), American Parkinson Disease Association (APDA-5589562), Alzheimer's Association (AARG-NTF-20-685694), New Vision Research (CCAD2020-002), Brightfocus Foundation (A2022031S), and the Brain and Behavior Research Foundation (NARSAD 26845) to KTB, NIH T3 2GM008620 and NIH F30 DA056215 to MH, T32 GM136624 to KB and PD, and NSF GRFP DGE-1839285 to PD.

CODE AVAILABILITY: Code used for this work is available on GitHub (https://github.com/ktbartas/Bartas_et_al_eLife_2024).

COMPETING INTERESTS: The authors have nothing to disclose.

REFERENCES:

893 1. Bromberg-Martin, E. S., Matsumoto, M. & Hikosaka, O. Dopamine in Motivational Control:
894 Rewarding, Aversive, and Alerting. *Neuron* **68**, 815–834 (2010).
895 2. Lammel, S., Lim, B. K. & Malenka, R. C. Reward and aversion in a heterogeneous
896 midbrain dopamine system. *Neuropharmacology* **76**, 351–359 (2014).
897 3. Wise, R. A. Dopamine, learning and motivation. *Nat Rev Neurosci* **5**, 483–494 (2004).
898 4. Kim, C. K. *et al.* Simultaneous fast measurement of circuit dynamics at multiple sites
899 across the mammalian brain. *Nat Methods* **13**, 325–8 (2016).
900 5. Lammel, S., Ion, D. I., Roeper, J. & Malenka, R. C. Report Projection-Specific Modulation
901 of Dopamine Neuron Synapses by Aversive and Rewarding Stimuli. *Neuron* **70**, 855–862
902 (2011).
903 6. Lammel, S. *et al.* Input-specific control of reward and aversion in the ventral tegmental
904 area. *Nature* **491**, 212–217 (2012).
905 7. Beier, K. T. *et al.* Circuit Architecture of VTA Dopamine Neurons Revealed by Systematic
906 Input-Output Mapping. *Cell* **162**, 622–634 (2015).
907 8. Menegas, W. *et al.* Dopamine neurons projecting to the posterior striatum form an
908 anatomically distinct subclass. *Elife* **4**, 1–30 (2015).
909 9. Watabe-Uchida, M., Zhu, L., Ogawa, S. K., Vamanrao, A. & Uchida, N. Whole-Brain
910 Mapping of Direct Inputs to Midbrain Dopamine Neurons. *Neuron* **74**, 858–873 (2012).
911 10. Beier, K. T. *et al.* Topological Organization of Ventral Tegmental Area Connectivity
912 Revealed by Viral-Genetic Dissection of Input-Output Relations. *Cell Rep* **26**, 159-167.e6
913 (2019).
914 11. Cardozo Pinto, D. F. *et al.* Characterization of transgenic mouse models targeting
915 neuromodulatory systems reveals organizational principles of the dorsal raphe. *Nat*
916 *Commun* **10**, (2019).
917 12. Faget, L. *et al.* Afferent Inputs to Neurotransmitter-Defined Cell Types in the Ventral
918 Tegmental Area. *Cell Rep* **15**, 2796–2808 (2016).
919 13. Kalivas, P. W. & Volkow, N. D. The neural basis of addiction: a pathology of motivation
920 and choice. *Am J Psychiatry* **162**, 1403–1413 (2005).
921 14. Hyman, S. E., Malenka, R. C. & Nestler, E. J. Neural mechanisms of addiction: the role of
922 reward-related learning and memory. *Annu Rev Neurosci* **29**, 565–598 (2006).
923 15. Beier, K. T. *et al.* Rabies screen reveals GPe control of cocaine-triggered plasticity.
924 *Nature* **549**, 345–350 (2017).
925 16. Tian, G. *et al.* An extended Amygdal-midbrain circuit controlling cocaine withdrawal-
926 induced anxiety and reinstatement. *Cell Rep* **39**, 1–16 (2022).
927 17. Juarez, B. & Han, M. H. Diversity of Dopaminergic Neural Circuits in Response to Drug
928 Exposure. *Neuropsychopharmacology* **41**, 2424–2446 (2016).
929 18. Mahler, S. V *et al.* Chemogenetic Manipulations of Ventral Tegmental Area Dopamine
930 Neurons Reveal Multifaceted Roles in Cocaine Abuse. *Journal of Neuroscience* **39**, 503–
931 518 (2019).
932 19. Saal, D., Dong, Y., Bonci, A. & Malenka, R. C. Drugs of abuse and stress trigger a
933 common synaptic adaptation in dopamine neurons. *Neuron* **37**, 577–582 (2003).
934 20. Ungless, M. A., Whistler, J. L., Malenka, R. C. & Bonci, A. Single cocaine exposure in
935 vivo induces long-term potentiation in dopamine neurons. *Nature* **411**, 583–7. (2001).

21. Niehaus, J. L., Murali, M. & Kauer, J. A. Drugs of abuse and stress impair LTP at inhibitory synapses in the ventral tegmental area. *European Journal of Neuroscience* **32**, 108–117 (2010).
22. Bocklisch, C. *et al.* Cocaine Disinhibits Dopamine Neurons by Potentiation of GABA Transmission in the Ventral Tegmental Area. *Science (1979)* **341**, 1521–1525 (2013).
23. Dong, Y. *et al.* Cocaine-induced potentiation of synaptic strength in dopamine neurons: behavioral correlates in GluRA(-/-) mice. *Proc Natl Acad Sci U S A* **101**, 14282–14287 (2004).
24. Creed, M. *et al.* Cocaine exposure enhances the activity of ventral tegmental area dopamine neurons via calcium-impermeable NMDARs. *Journal of Neuroscience* **36**, 10759–10768 (2016).
25. Tian, G. *et al.* An extended Amygdala-midbrain circuit controlling cocaine withdrawal-induced anxiety and reinstatement. *Cell Rep* **39**, 1–16 (2022).
26. Backman, C. M. *et al.* Characterization of a mouse strain expressing Cre recombinase from the 3' untranslated region of the dopamine transporter locus. *Genesis* **44**, 383–390 (2006).
27. Taniguchi, H. *et al.* A Resource of Cre Driver Lines for Genetic Targeting of GABAergic Neurons in Cerebral Cortex. *Neuron* **71**, 995–1013 (2011).
28. Vong, L. *et al.* Leptin Action on GABAergic Neurons Prevents Obesity and Reduces Inhibitory Tone to POMC Neurons. *Neuron* **71**, 142–154 (2011).
29. Kumar, N. *et al.* The development of an AAV-based crispr sacas9 genome editing system that can be delivered to neurons in vivo and regulated via doxycycline and cre-recombinase. *Front Mol Neurosci* **11**, 1–14 (2018).
30. Pedregosa, F. *et al.* Scikit-learn: Machine Learning in Python. *Journal of Machine Learning Research* **12**, 2825–2830 (2011).
31. McInnes, L., Healy, J. & Melville, J. UMAP: Uniform Manifold Approximation and Projection for Dimension Reduction. *ArXiv* **1802.03426**, 1–51 (2018).
32. Derdeyn, P., Hui, M., Macchia, D. & Beier, K. Uncovering the Connectivity Logic of the Ventral Tegmental Area. *Front Neural Circuits* **15**, 799688 (2022).
33. Waskom, M. Seaborn: Statistical Data Visualization. *J Open Source Softw* **6**, 3021 (2021).
34. Hunter, J. D. Matplotlib: a 2D graphics environment. *Comput Sci Eng* **9**, 90–95 (2007).
35. Chon, U., Vanselow, D. J., Cheng, K. C. & Kim, Y. Enhanced and unified anatomical labeling for a common mouse brain atlas. *Nat Commun* **10**, (2019).
36. Oh, S. W. *et al.* A mesoscale connectome of the mouse brain. *Nature* **508**, 207–214 (2014).
37. Lein, E. S. *et al.* Genome-wide atlas of gene expression in the adult mouse brain. *Nature* **445**, 168–176 (2007).
38. Brynildsen, J. K. *et al.* Gene coexpression patterns predict opiate-induced brain-state transitions. *Proc Natl Acad Sci U S A* **117**, 19556–19565 (2020).
39. Fulcher, B. D., Murray, J. D., Zerbi, V. & Wang, X. J. Multimodal gradients across mouse cortex. *Proc Natl Acad Sci U S A* **116**, 4689–4695 (2019).

40. Sian, J., Youdim, M. & Riederer, P, et al. Biochemical Anatomy of the Basal Ganglia and Associated Neural Systems. in *Basic Neurochemistry: Molecular, Cellular and Medical Aspects.* (eds. Siegel, G., Agranoff, B. & Albers, RW, et al.) (1999).
41. Xie, Z. *et al.* Gene Set Knowledge Discovery with Enrichr. *Curr Protoc* **1**, 1–51 (2021).
42. Ji, X., Zhang, H. & Cui, Q. A Panel of Synapse-Related Genes as a Biomarker for Gliomas. *Front Neurosci* **14**, 1–8 (2020).
43. Wang, R. *et al.* Ion channel gene expression predicts survival in glioma patients. *Sci Rep* **5**, 1–10 (2015).
44. Berchtold, N. C. *et al.* Synaptic genes are extensively downregulated across multiple brain regions in normal human aging and Alzheimer's disease. *Neurobiol Aging* **34**, 1653–1661 (2013).
45. Shi, L. *et al.* AddictGene: An integrated knowledge base for differentially expressed genes associated with addictive substance. *Comput Struct Biotechnol J* **19**, 2416–2422 (2021).
46. Saheki, Y. & De Camilli, P. Synaptic vesicle endocytosis. *Cold Spring Harb Perspect Biol* **4**, (2012).
47. Harding, S. D. *et al.* The IUPHAR/BPS guide to PHARMACOLOGY in 2022: Curating pharmacology for COVID-19, malaria and antibacterials. *Nucleic Acids Res* **50**, D1282–D1294 (2022).
48. Yamaguchi, T., Wang, H. L., Li, X., Ng, T. H. & Morales, M. Mesocorticolimbic glutamatergic pathway. *Journal of Neuroscience* **31**, 8476–8490 (2011).
49. Yamaguchi, T., Sheen, W. & Morales, M. Glutamatergic neurons are present in the rat ventral tegmental area. *European Journal of Neuroscience* **25**, 106–118 (2007).
50. Root, D. H. *et al.* Single rodent mesohabenular axons release glutamate and GABA. *Nat Neurosci* **17**, 1543–1551 (2014).
51. Morales, M. & Margolis, E. B. Ventral tegmental area: Cellular heterogeneity, connectivity and behaviour. *Nat Rev Neurosci* **18**, 73–85 (2017).
52. Hnasko, T. S., Hjelmstad, G. O., Fields, H. L. & Edwards, R. H. Ventral tegmental area glutamate neurons: electrophysiological properties and projections. *Journal of Neuroscience* **32**, 15076–15085 (2012).
53. Kim, J. I. *et al.* Aldehyde dehydrogenase 1a1 mediates a GABA synthesis pathway in midbrain dopaminergic neurons. *Science (1979)* **350**, 102–106 (2015).
54. Tritsch, N. X., Ding, J. B. & Sabatini, B. L. Dopaminergic neurons inhibit striatal output through non-canonical release of GABA. *Nature* **490**, 262–266 (2012).
55. Koob, G. F. A Role for Brain Stress Systems in Addiction. *Neuron* **59**, 11–34 (2008).
56. Koob, G. F. Brain stress systems in the amygdala and addiction. *Brain Res* **1293**, 61–75 (2009).
57. Tian, G. *et al.* Molecular and circuit determinants in the globus pallidus mediating control of cocaine-induced behavioral plasticity. *Neuron* **112**, 3470-3485.e12 (2024).
58. Lammel, S. *et al.* Unique Properties of Mesoprefrontal Neurons within a Dual Mesocorticolimbic Dopamine System. *Neuron* **57**, 760–773 (2008).
59. Larson, M. H. *et al.* CRISPR interference (CRISPRi) for sequence-specific control of gene expression. *Nat Protoc* **8**, 2180–2196 (2013).

1021 60. Li, H. *et al.* Entopeduncular nucleus projections to the lateral habenula contribute to
1022 cocaine avoidance. *Journal of Neuroscience* **41**, 298–306 (2021).
1023 61. López, A. J. *et al.* Medial habenula cholinergic signaling regulates cocaine-associated
1024 relapse-like behavior. *Addiction Biology* **24**, 403–413 (2019).
1025 62. Tan, D., Nuno-Perez, A., Mameli, M. & Meye, F. J. Cocaine withdrawal reduces GABABR
1026 transmission at entopeduncular nucleus – lateral habenula synapses. *European Journal*
1027 *of Neuroscience* **50**, 2124–2133 (2019).
1028 63. Koob, G. F. & Volkow, N. D. Neurocircuitry of addiction. *Neuropsychopharmacology* **35**,
1029 217–238 (2010).
1030 64. Marchant, N. J., Zayra Millan, E. & McNally, G. P. The hypothalamus and the
1031 neurobiology of drug seeking. *Cellular and Molecular Life Sciences* vol. 69 581–597
1032 Preprint at https://doi.org/10.1007/s00018-011-0817-0 (2012).
1033 65. Sheng, H. *et al.* Nucleus accumbens circuit disinhibits lateral hypothalamus glutamatergic
1034 neurons contributing to morphine withdrawal memory in male mice. *Nat Commun* **14**,
1035 (2023).
1036 66. DiLeone, R. J., Georgescu, D. & Nestler, E. J. Lateral hypothalamic neuropeptides in
1037 reward and drug addiction. in *Life Sciences* vol. 73 759–768 (Elsevier Inc., 2003).
1038 67. Aston-Jones, G., Smith, R. J., Moorman, D. E. & Richardson, K. A. Role of lateral
1039 hypothalamic orexin neurons in reward processing and addiction. *Neuropharmacology*
1040 vol. 56 112–121 Preprint at https://doi.org/10.1016/j.neuropharm.2008.06.060 (2009).
1041 68. He, T. *et al.* A novel cholinergic projection from the lateral parabrachial nucleus and its
1042 role in methamphetamine-primed conditioned place preference. *Brain Commun* **4**, (2022).
1043 69. Pyeon, G. H., Kim, J. H., Choi, J. S. & Jo, Y. S. Activation of CGRP neurons in the
1044 parabrachial nucleus suppresses addictive behavior. *Proc Natl Acad Sci U S A* **121**,
1045 (2024).
1046 70. Tian G *et al.* Molecular and circuit determinants in the globus pallidus mediating control of
1047 cocaine-induced behavioral plasticity. *Neuron Sneak Peek*
1048 https://papers.ssrn.com/sol3/papers.cfm?abstract_id=4549829 (2023).
1049 71. Liu, Y., Lin, D., Wu, B. & Zhou, W. Ketamine abuse potential and use disorder. *Brain Res*
1050 *Bull* **126**, 68–73 (2016).
1051 72. Ni, A., Lee Cantrell, F. & Clark, R. F. Ketamine exposure demographics and outcomes
1052 over 16 years as reported to US poison centers. *American Journal of Emergency*
1053 *Medicine* **36**, 1459–1462 (2018).
1054 73. Dillon, P., Copeland, J. & Jansen, K. Patterns of use and harms associated with non-
1055 medical ketamine use. *Drug Alcohol Depend* **69**, 23–28 (2003).
1056 74. Morgan, C. J. A. & Curran, H. V. Ketamine use: A review. *Addiction* **107**, 27–38 (2012).
1057 75. Ryder, S., Way, W. L. & Trevor, A. J. Comparative pharmacology of the optical isomers of
1058 ketamine in mice. *Eur J Pharmacol* **49**, 15–23 (1978).
1059 76. Finck, A. D. & Ngai, S. H. Opiate receptor mediation of ketamine analgesia. *Anesth Analg*
1060 **56**, 291–297 (1982).
1061 77. Hustveit, O., Maurset, A. & Oye, I. Interaction of the Chiral Forms of Ketamine with
1062 Opioid, Phencyclidine, c and Muscarinic Receptors. *Pharmacol Toxicol* **77**, 355–359
1063 (1995).

78. Bonaventura, J. *et al.* Pharmacological and behavioral divergence of ketamine enantiomers:implications for abuse liability. *Mol Psychiatry* **26**, 6704–6722 (2021).
79. Williams, N. R. *et al.* Attenuation of antidepressant and antisuicidal effects of ketamine by opioid receptor antagonism. *Mol Psychiatry* **24**, 1779–1786 (2019).
80. Williams, N. R. *et al.* Attenuation of antidepressant effects of ketamine by opioid receptor antagonism. *American Journal of Psychiatry* **175**, 1205–1215 (2018).
81. Gelernter, J. *et al.* Genome-wide association study of opioid dependence: Multiple associations mapped to calcium and potassium pathways. *Biol Psychiatry* **76**, 66–74 (2014).
82. Malcolm, R., Brady, K. T., Moore, J. & Kajdasz, D. Amlodipine treatment of cocaine dependence. *J Psychoactive Drugs* **31**, 117–120 (1999).
83. Altamura, A. C., Regazzetti, M. G. & Porta, M. Nimodipine in human alcohol withdrawal syndrome - an open study. *European Neuropsychopharmacology* **1**, 37–40 (1990).
84. Rosse, R. *et al.* Nimodipine Pharmacotherapeutic Adjuvant Therapy for Inpatient Treatment of Cocaine Dependence. *Clin Neuropharmacol* **17**, 348–358 (1994).
85. Muntaner, C., Kumor, K., Nagoshi, C. & Jaffe, J. Effect of nifedipine pretreatment on subjective and cardiovascular responses to intravenous cocaine in humans. *Drug Alcohol Depend* **105**, 37–41 (1991).
86. Johnson, B. A. *et al.* Effects of Isradipine on Cocaine-Induced Subjective Mood. *J Clin Psychopharmacol* **24**, 180–191 (2004).
87. Vaupel, D. B., Lange, W. R. & London, E. D. Effects of verapamil on morphine-induced euphoria, analgesia and respiratory depression in humans. *Journal of Pharmacology and Experimental Therapeutics* **267**, 1386–1394 (1993).

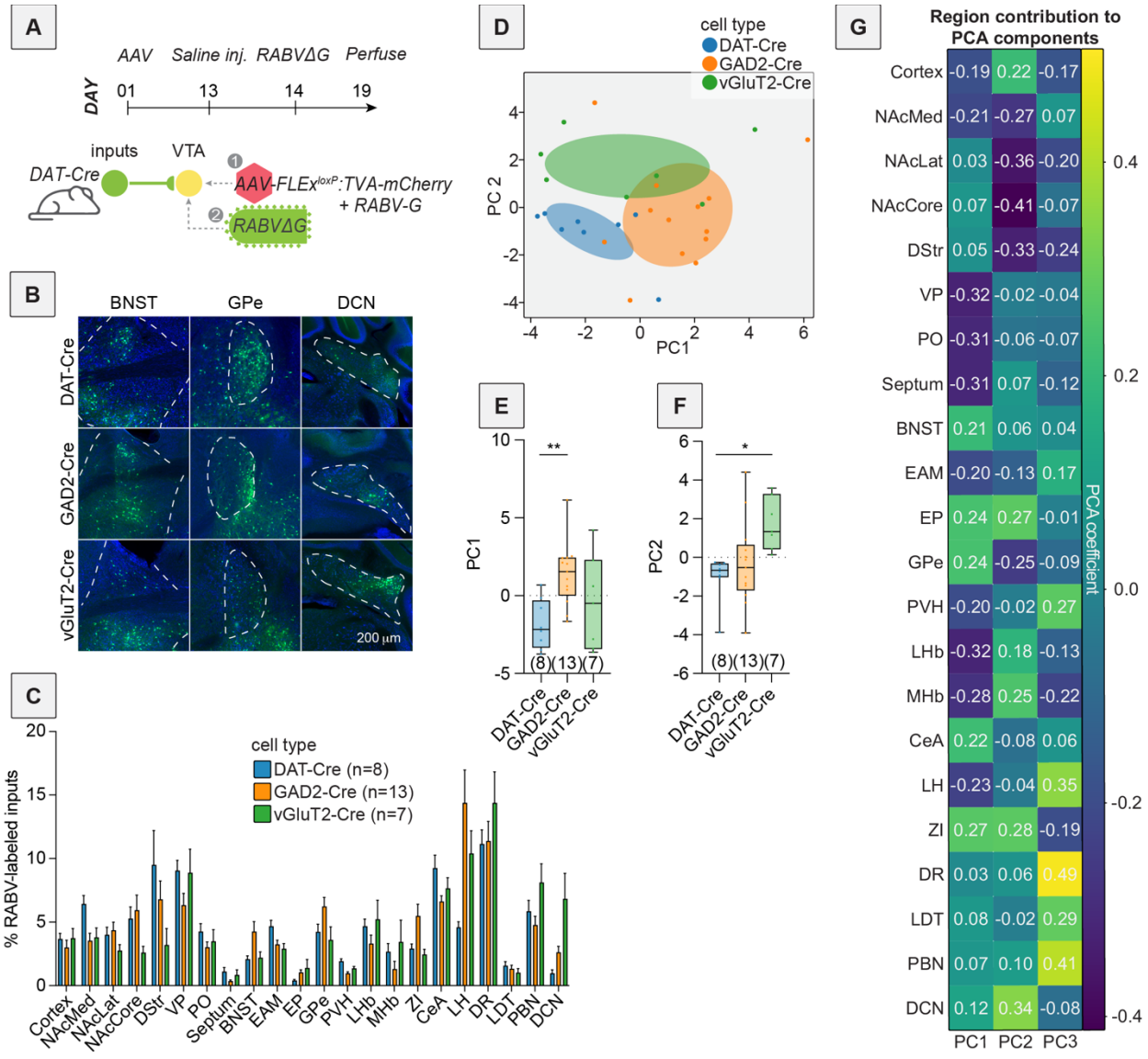
A
AAV
Saline inj.
RABVΔG
Perfuse
DAY
01
13
14
19
inputs
VTA
DAT-Cre
AAV-FLEx^loxP:TVA-mCherry
+ RABV-G
RABVΔG
B
BNST
GPe
DCN
DAT-Cre
GAD2-Cre
vGluT2-Cre
200 µm
C
% RABV-labeled inputs
cell type
DAT-Cre (n=8)
GAD2-Cre (n=13)
vGluT2-Cre (n=7)
Cortex
NAcMed
NAcLat
NAcCore
DStr
VP
PO
Septum
BNST
EAM
EP
GPe
PVH
LHb
MHb
ZI
CeA
LH
DR
LDT
PBN
DCN
D
cell type
DAT-Cre
GAD2-Cre
vGluT2-Cre
PC 2
PC1
E
PC1
**
(8)(13)(7)
DAT-Cre
GAD2-Cre
vGluT2-Cre
F
PC2
*
(8)(13)(7)
DAT-Cre
GAD2-Cre
vGluT2-Cre
G
Region contribution to PCA components
Cortex -0.19 0.22 -0.17
NAcMed -0.21 -0.27 0.07
NAcLat 0.03 -0.36 -0.20
NAcCore 0.07 -0.41 -0.07
DStr 0.05 -0.33 -0.24
VP -0.32 -0.02 -0.04
PO -0.31 -0.06 -0.07
Septum -0.31 0.07 -0.12
BNST 0.21 0.06 0.04
EAM -0.20 -0.13 0.17
EP 0.24 0.27 -0.01
GPe 0.24 -0.25 -0.09
PVH -0.20 -0.02 0.27
LHb -0.32 0.18 -0.13
MHb -0.28 0.25 -0.22
CeA 0.22 -0.08 0.06
LH -0.23 -0.04 0.35
ZI 0.27 0.28 -0.19
DR 0.03 0.06 0.49
LDT 0.08 -0.02 0.29
PBN 0.07 0.10 0.41
DCN 0.12 0.34 -0.08
PC1 PC2 PC3
PCA coefficient

1089

1090 **Figure 1: PCA-based dimensionality reduction of RABV input tracing to 3 different VTA cell**
1091 **types.**
1092 (A) Schematic and timeline of viral injections into mice.
1093 (B) Representative images of the BNST, GPe, and DCN of DAT-Cre, GAD2-Cre, and vGlut2-Cre
1094 mice. Green indicates RABV-labeled cells. Scale, 200 μm.
1095 (C) Bar plot showing percent of RABV-labeled cells in each input region for DAT-Cre, GAD2-Cre,
1096 and vGlut2-Cre mice.
1097 (D) PCA of input labeling from brains from DAT-Cre, GAD2-Cre, and vGlut2-Cre mice. For this
1098 and other figures, ellipsoids were centered at the average coordinate of a condition and stretched
1099 one standard deviation along the primary and secondary axes.
1100 (E) Box plot comparisons of PC1. One-way ANOVA $p = 0.010$, pairwise t-tests DAT-Cre vs.
1101 GAD2-Cre multiple comparisons adjusted $p = 0.0087$, DAT-Cre vs. vGluT2-Cre $p = 0.46$, GAD2-
1102 Cre vs. vGluT2-Cre $p = 0.19$. n=8 for DAT-Cre, n = 13 for GAD2-Cre, and n = 7 for vGluT2-Cre.
1103 (F) Box plot comparisons of PC2. One-way ANOVA $p = 0.016$, pairwise t-tests DAT-Cre vs.
1104 GAD2-Cre multiple comparisons adjusted $p = 0.65$, DAT-Cre vs. vGluT2-Cre $p = 0.016$, GAD2-
1105 Cre vs. vGluT2-Cre $p = 0.051$.
1106 (G) Heatmap of the contributions of each brain region, or feature, in the data to PCs 1 through 3.
1107 For this and all figures, error bars = ± 1 SEM, * $p < 0.05$, ** $p < 0.01$, *** $p < 0.001$, **** $p < 0.0001$.

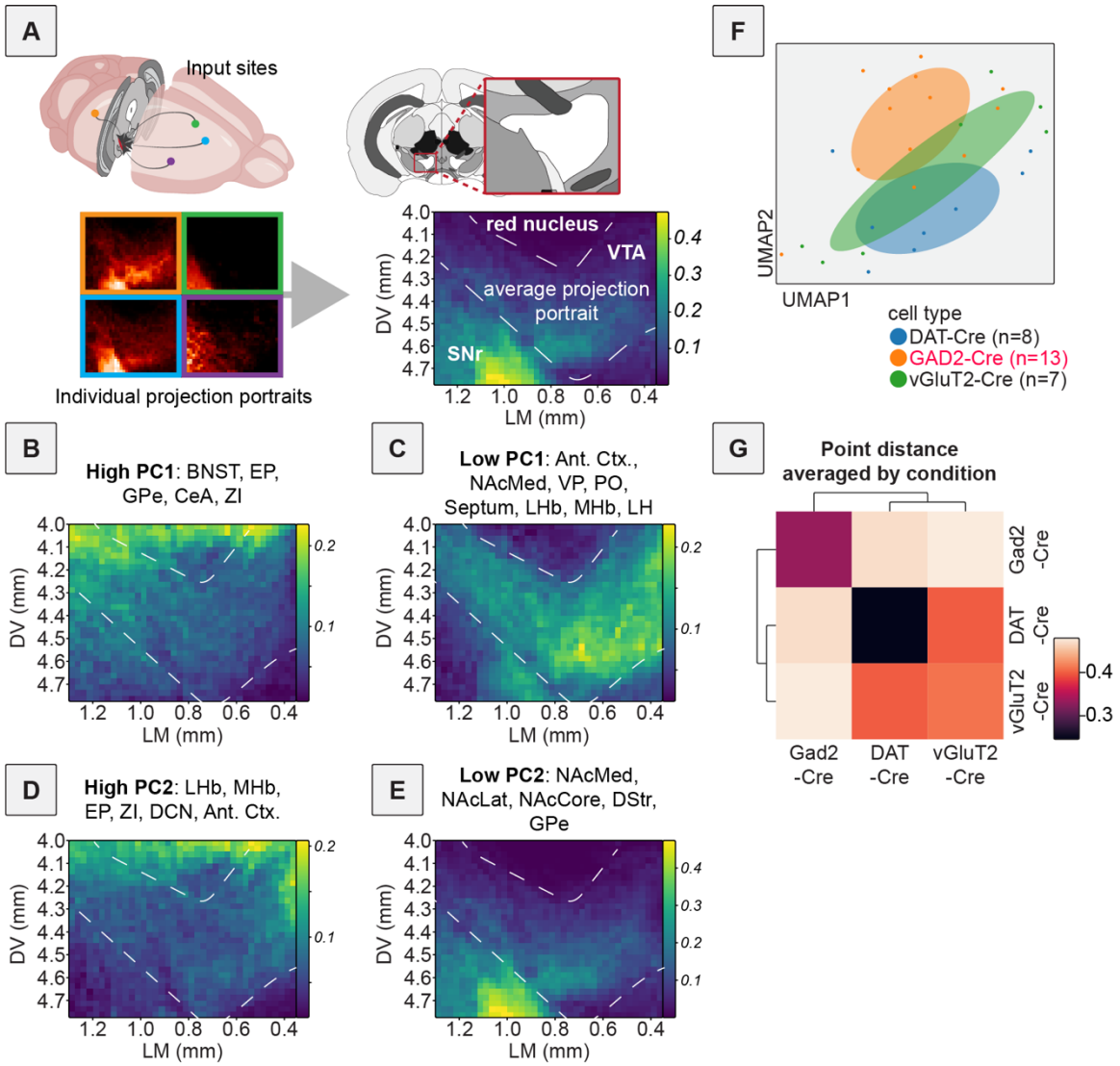

Figure 2: Projection portraits and UMAP of RABV inputs to VTA cells.

(A) Schematic of how projection portraits are constructed. A representative slice of the VTA is considered for experiments from the Allen Mouse Brain Connectivity Atlas with injections into relevant brain regions that provide input to the VTA. Projection density values in this slice are averaged and visualized to obtain the projection portrait in the VTA for that group of regions.

(B) Projection portrait of the VTA based on inputs from regions with a high positive contribution to PC1: BNST, EP, GPe, CeA, and ZI.

(C) Projection portrait of the VTA based on inputs from regions with a large negative contribution to PC1: anterior cortex, NAcMed, VP, PO, septum, LHb, MHb, and LH.

(D) Projection portrait of the VTA based on inputs from regions with a high positive contribution to PC2: LHb, MHb, EP, ZI, DCN, and anterior cortex.

1120 (E) Projection portrait of the VTA based on inputs from regions with a large negative contribution
1121 to PC2: NAcMed, NAcLat, NAcCore, DStr, and GPe.
1122 (F) UMAP embedding of input labeling of brains from DAT-Cre, GAD2-Cre, and vGlut2-Cre mice.
1123 (G) Correlogram generated using the average Euclidean distance of data points from each other
1124 from 20 UMAP embeddings.

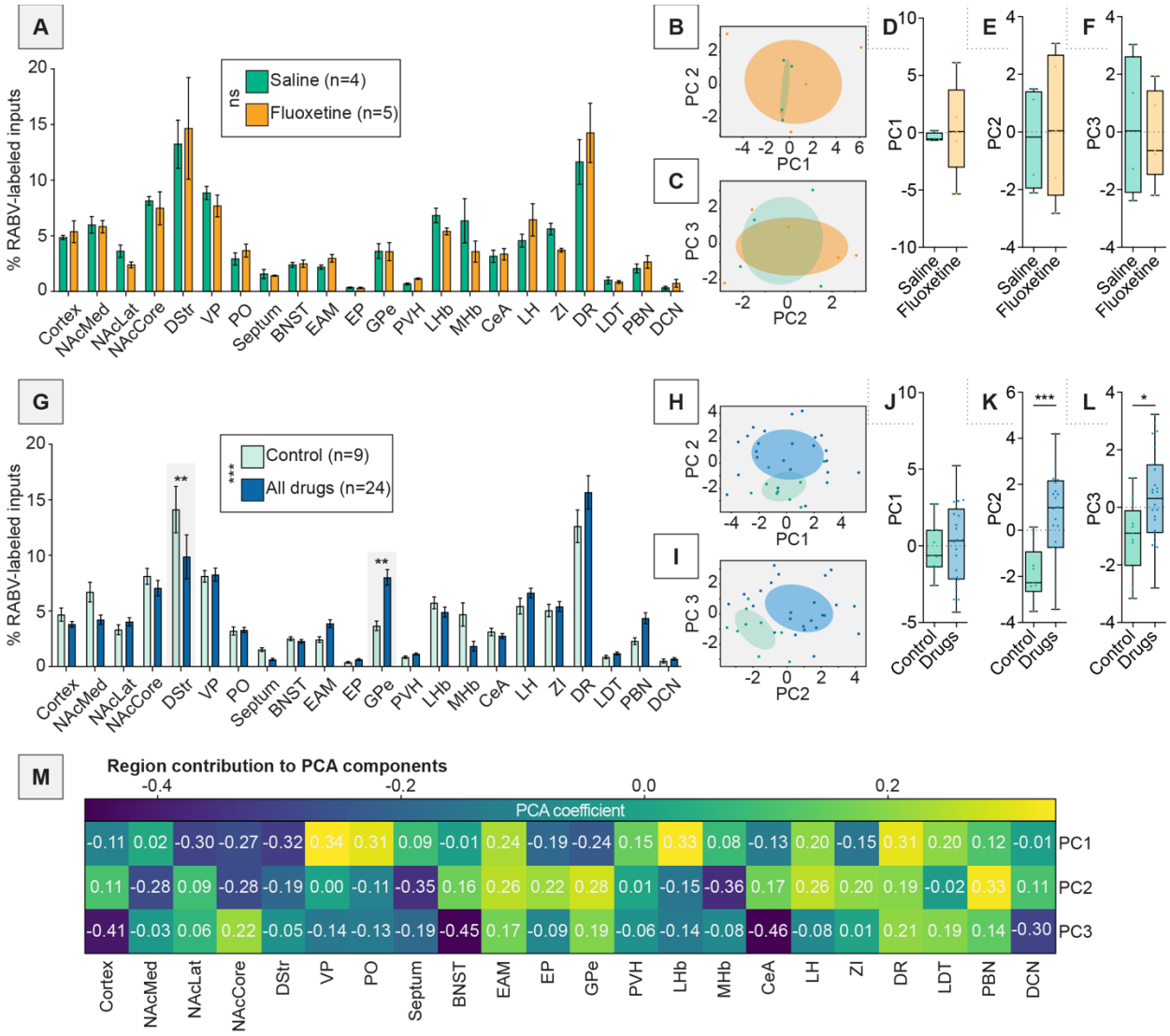

Figure 3: PCA can deconvolve drug-induced effects from experimental variation.

(A) Bar graph representation of inputs from DAT-Cre mice anesthetized with isoflurane and treated with a single injection of saline or fluoxetine. n = 4 for saline, n = 5 for fluoxetine. Two-way ANOVA interaction term p = 0.9365.

(B) PCA plot showing PC1 and PC2 of brains from saline or fluoxetine-treated mice.

(C) PCA plot showing PC2 and PC3 of brains from saline or fluoxetine-treated mice.

(D) Box plot of PC1, p = 0.75. n = 4 for saline, n = 5 for fluoxetine.

(E) Box plot of PC2, p = 0.78.

(F) Box plot of PC3, p = 0.81.

(G) Bar graph representation of inputs from DAT-Cre mice anesthetized with isoflurane and treated with a single injection of saline or fluoxetine (controls), or one of the addictive drugs cocaine, methamphetamine, amphetamine, nicotine, or morphine. n = 9 for control, n = 24 for

1138 combined addictive drugs. Two-way ANOVA, interaction term $p = 0.0001$; unpaired t-tests with
1139 Sidak corrections for multiple comparisons DStr $p = 0.0051$, GPe $p = 0.0036$.
1140 (H) PCA plot showing PC1 and PC2 of brains from control or drug-treated mice.
1141 (I) PCA plot showing PC2 and PC3 of brains from control or drug-treated mice.
1142 (J) Box plot of PC1, $p = 0.78$. $n = 9$ for control, $n = 24$ for drugs.
1143 (K) Box plot of PC2, $p = 0.0009$.
1144 (L) Box plot of PC3, $p = 0.024$.
1145 (M) Heatmap of the contributions of each brain region to PC1 through PC3 for data shown in
1146 panels H-I.

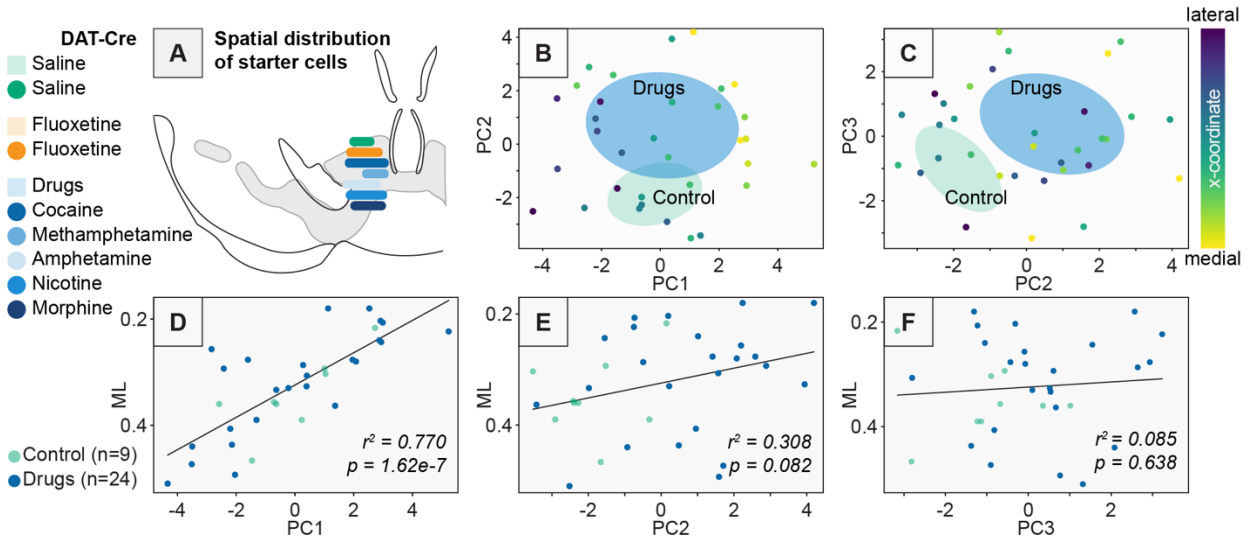

Figure 4: Differences in starter cell location do not explain differences in RABV input labeling patterns between addictive drug and control groups.

(A) Distribution of the starter cell center of mass along the medial-lateral axis for each experimental condition. Saline n = 4, fluoxetine n = 5, cocaine n = 5, methamphetamine n = 4, amphetamine n = 5, nicotine n = 5, morphine n = 5.

(B) PC1 vs. PC2 for control vs. drug conditions as shown in **Figure 3H**, with each point colored according to the medial-lateral coordinate of the center of mass of starter cells for each brain.

(C) PC2 vs. PC3 for control vs. drug conditions as shown in **Figure 3I**, with each point colored according to the medial-lateral coordinate of the center of mass of starter cells for each brain.

(D) Linear regression between the x-coordinate of the center of mass of starter cells for each brain vs. PC1. $r^2 = 0.770$, $p = 1.62e-7$,

(E) Linear regression between the x-coordinate of the center of mass of starter cells for each brain vs. PC2. $r^2 = 0.308$, $p = 0.082$.

(F) Linear regression between the x-coordinate of the center of mass of starter cells for each brain vs. PC3, $r^2 = 0.085$, $p = 0.638$.

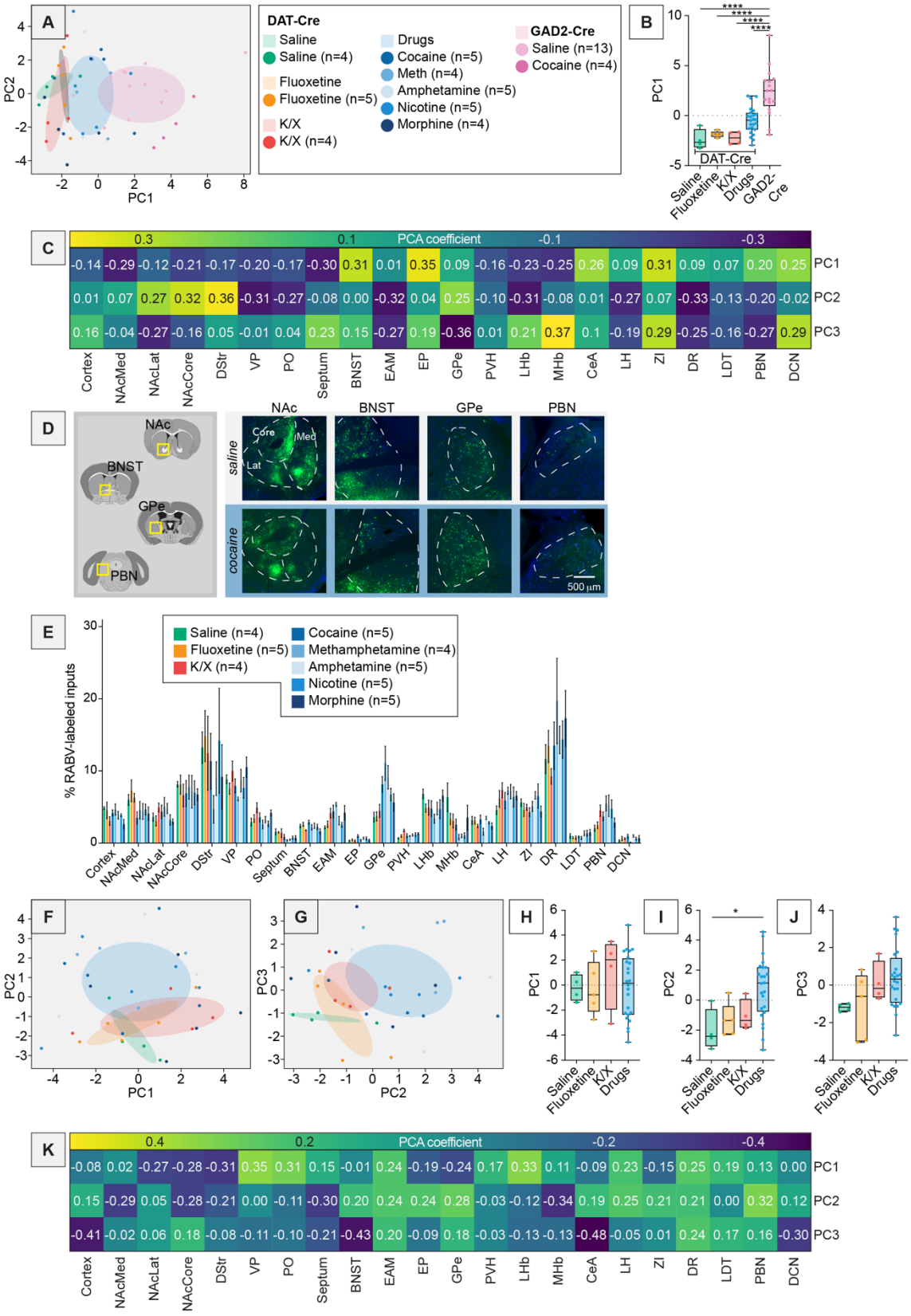
A
PC2
PC1
DAT-Cre
Saline
Saline (n=4)
Fluoxetine
Fluoxetine (n=5)
K/X
K/X (n=4)
Drugs
Cocaine (n=5)
Meth (n=4)
Amphetamine (n=5)
Nicotine (n=5)
Morphine (n=4)
GAD2-Cre
Saline (n=13)
Cocaine (n=4)
B
PC1
DAT-Cre
Saline
Fluoxetine
K/X
Drugs
GAD2-Cre
C
PCA coefficient
0.3
0.1
-0.1
-0.3
PC1
PC2
PC3
Cortex
NAcMed
NAcLat
NAcCore
DStr
VP
PO
Septum
BNST
EAM
EP
GPe
PVH
LHb
MHb
CeA
LH
ZI
DR
LDT
PBN
DCN
D
NAc
BNST
GPe
PBN
Core
Med
Lat
saline
cocaine
500 µm
E
% RABV-labeled inputs
Saline (n=4)
Fluoxetine (n=5)
K/X (n=4)
Cocaine (n=5)
Methamphetamine (n=4)
Amphetamine (n=5)
Nicotine (n=5)
Morphine (n=5)
F
G
H
I
J
K
PCA coefficient
0.4
0.2
-0.2
-0.4

1163

1164 **Figure 5: Dimensionality reduction analysis of brains from animals treated with a single**
1165 **drug exposure.**
1166 (A) PCA plot showing PC1 and PC2 of brains from DAT-Cre and GAD2-Cre mice. DAT-Cre mice
1167 were anesthetized with K/X and treated with saline or anesthetized with isoflurane and treated
1168 with saline or one of the drugs cocaine, methamphetamine, amphetamine, nicotine, morphine, or
1169 fluoxetine. GAD2-Cre mice were anesthetized with isoflurane and treated with saline or cocaine.
1170 (B) Box plot of PC1, One-way ANOVA $p < 0.0001$, pairwise t-tests DAT-Cre saline vs. DAT-Cre
1171 fluoxetine multiple comparisons adjusted $p = 0.99$, DAT-Cre saline vs. DAT-Cre K/X $p = 1.0$, DAT-
1172 Cre saline vs. DAT-Cre drugs $p = 0.23$, DAT-Cre saline vs. GAD2-Cre $p < 0.0001$, DAT-Cre
1173 fluoxetine vs. DAT-Cre K/X $p = 1.0$, DAT-Cre fluoxetine vs. DAT-Cre drugs $p = 0.46$, DAT-Cre
1174 fluoxetine vs. GAD2-Cre $p < 0.0001$, DAT-Cre K/X vs. DAT-Cre drugs $p = 0.31$, DAT-Cre K/X vs.
1175 GAD2-Cre $p < 0.0001$, DAT-Cre drugs vs. GAD2-Cre $p < 0.0001$. $n = 4$ for DAT-Cre saline and
1176 DAT-Cre K/X, $n = 5$ for DAT-Cre fluoxetine, $n = 24$ for DAT-Cre drugs, $n = 17$ for GAD2-Cre.
1177 (C) Heatmap of the contributions of each brain region to PC1 through PC3 for data shown in panel
1178 A.
1179 (D) Representative images of brain slices from DAT-Cre mice showing, from left to right, the NAc,
1180 BNST, GPe, and PBN. Scale, 500 μm.
1181 (E) Bar plot showing percentage of RABV-labeled cells in each input region for the DAT-Cre mice
1182 shown in panel A.
1183 (F) PCA plot showing PC1 and PC2 of brains from DAT-Cre mice anesthetized with isoflurane
1184 and treated with cocaine, methamphetamine, amphetamine, nicotine, morphine, fluoxetine, or
1185 saline, or anesthetized with K/X and treated with saline.
1186 (G) PC2 and PC3 of the same group of brains as shown in panel F.
1187 (H) Box plot of PC1, One-way ANOVA $p = 0.81$.
1188 (I) Box plot of PC2, One-way ANOVA $p = 0.0093$, pairwise t-tests DAT-Cre saline vs. DAT-Cre
1189 fluoxetine multiple comparisons adjusted $p = 0.94$, DAT-Cre saline vs. DAT-Cre K/X $p = 0.87$,
1190 DAT-Cre saline vs. DAT-Cre drugs $p = 0.034$, DAT-Cre fluoxetine vs. DAT-Cre K/X $p = 0.99$, DAT-
1191 Cre fluoxetine vs. DAT-Cre drugs $p = 0.10$, DAT-Cre K/X vs. DAT-Cre drugs $p = 0.27$.
1192 (J) Box plot of PC3, One-way ANOVA $p = 0.086$.
1193 (K) Heatmap of the contributions of each brain region to PC1 through PC3 for data shown in
1194 panels F and G.

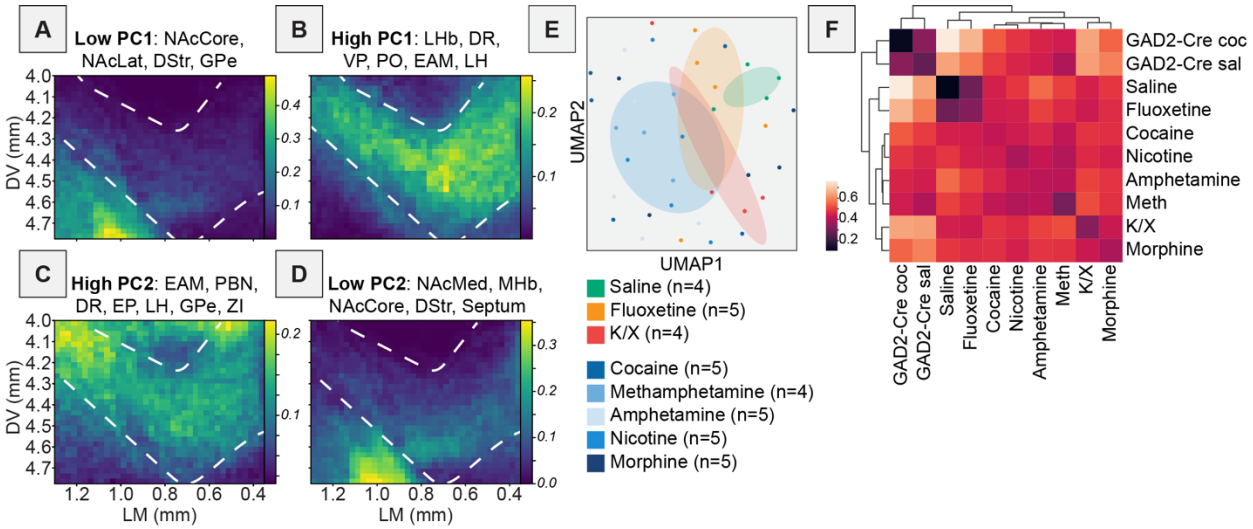

Figure 6: Projection portraits and UMAP plot of VTA^{DA} cells following a single drug exposure.

(A) Projection portrait of the VTA based on inputs from regions with a large negative contribution to PC1, based on data from **Figure 5K**: NAcCore, NAcLat, DStr, GPe.

(B) Projection portrait based on inputs from regions with a high positive contribution to PC1, based on data from **Figure 5K**: LHb, DR, VP, PO, EAM, LH.

(C) Projection portrait based on inputs from regions with a high positive contribution to PC2, based on data from **Figure 5K**: EAM, PBN, DR, EP, LH, GPe, ZI.

(D) Projection portrait based on inputs from regions with a large negative contribution to PC2, based on data from **Figure 5K**: NAcMed, NAcCore, DStr, Septum, MHb.

(E) UMAP embedding of data from the brains of DAT-Cre mice shown in **Figure 5E**.

(F) Correlogram showing average Euclidean distance of data points over 20 UMAP embeddings of the data presented in panel E.

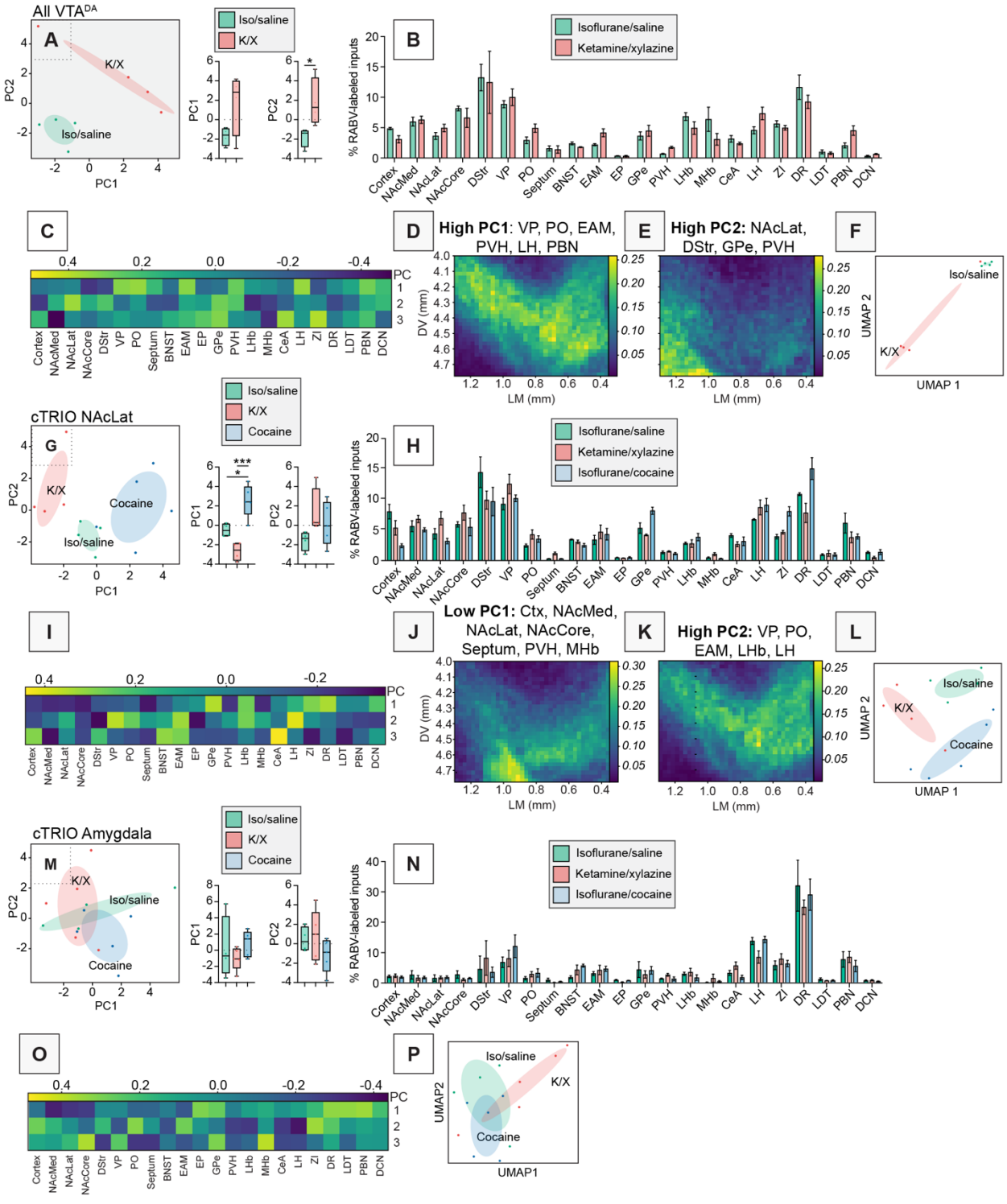

Figure 7: Dimensionality reduction analysis of brains from animals anesthetized with isoflurane and treated with either cocaine or saline, or anesthetized with ketamine/xylazine and treated with saline.

1213 (A) PCA plot of input data from VTA^{DA} cells from mice anesthetized either with isoflurane or K/X
1214 and given saline. Box plot comparisons of PC1 and PC2 are shown to the right. PC1, $p = 0.086$,
1215 PC2, $p = 0.037$, unpaired t-tests. $n = 4$ for both.
1216 (B) Bar plot showing percentage of RABV-labeled cells in each input region from mice
1217 anesthetized either with isoflurane or K/X and given saline.
1218 (C) Heatmap of the contributions from each brain region to PC1 to PC3 for data shown in panel
1219 A.
1220 (D) Projection portrait of regions with high PC1 contributions in all VTA^{DA} cells: VP, PO, EAM,
1221 PVH, LH, PBN.
1222 (E) Projection portrait of regions with high PC2 contributions in VTA^{DA} cells: NAcLat, DStr, GPe,
1223 PVH.
1224 (F) UMAP plot of input data from VTA^{DA} cells from mice anesthetized either with isoflurane or K/X
1225 and given saline.
1226 (G) PCA plot of RABV input mapping experiments to $VTA^{DA}\rightarrow$NAcLat cells in mice anesthetized
1227 with isoflurane and given saline or cocaine, or anesthetized with K/X and given saline. Box plot
1228 comparisons of PC1 and PC2 are shown to the right. PC1, One-way ANOVA $p = 0.0003$, pairwise
1229 t-tests saline vs. cocaine multiple comparisons adjusted $p = 0.011$, saline vs. K/X $p = 0.071$, K/X
1230 vs. cocaine $p = 0.0002$. PC2, One-way ANOVA $p = 0.16$. $n=4$ for saline and K/X, $n = 5$ for cocaine.
1231 (H) Bar plot showing percent of RABV-labeled cells in each input region for cTRIO experiments
1232 from $VTA^{DA}\rightarrow$NAcLat cells.
1233 (I) Heatmap of the contributions from each brain region to PC1 to PC3 for data shown in panel G.
1234 (J) Projection portrait of regions with low PC1 contributions in $VTA^{DA}\rightarrow$NAcLat cells: cortex,
1235 NAcMed, NAcLat, NAcCore, septum, PVH, MHb.
1236 (K) Projection portrait of regions with high PC2 contributions in $VTA^{DA}\rightarrow$NAcLat cells: VP, PO,
1237 EAM, LHb, LH.
1238 (L) UMAP plot of input mapping experiments to $VTA^{DA}\rightarrow$NAcLat cells.
1239 (M) PCA plot of input mapping experiments to $VTA^{DA}\rightarrow$Amygdala cells. Box plot comparisons of
1240 PC1 and PC2 are shown to the right. PC1, One-way ANOVA $p = 0.48$. PC2, One-way ANOVA p
1241 $= 0.30$. $n=4$ for saline, $n = 5$ for K/X and cocaine.
1242 (N) Bar plot showing percent of RABV-labeled cells in each input region for cTRIO experiments
1243 from $VTA^{DA}\rightarrow$Amygdala cells.
1244 (O) Heatmap of the contributions of each brain region to PC1 to PC3 for data shown in panel M.
1245 (P) UMAP plot of input mapping experiments to $VTA^{DA}\rightarrow$Amygdala cells.

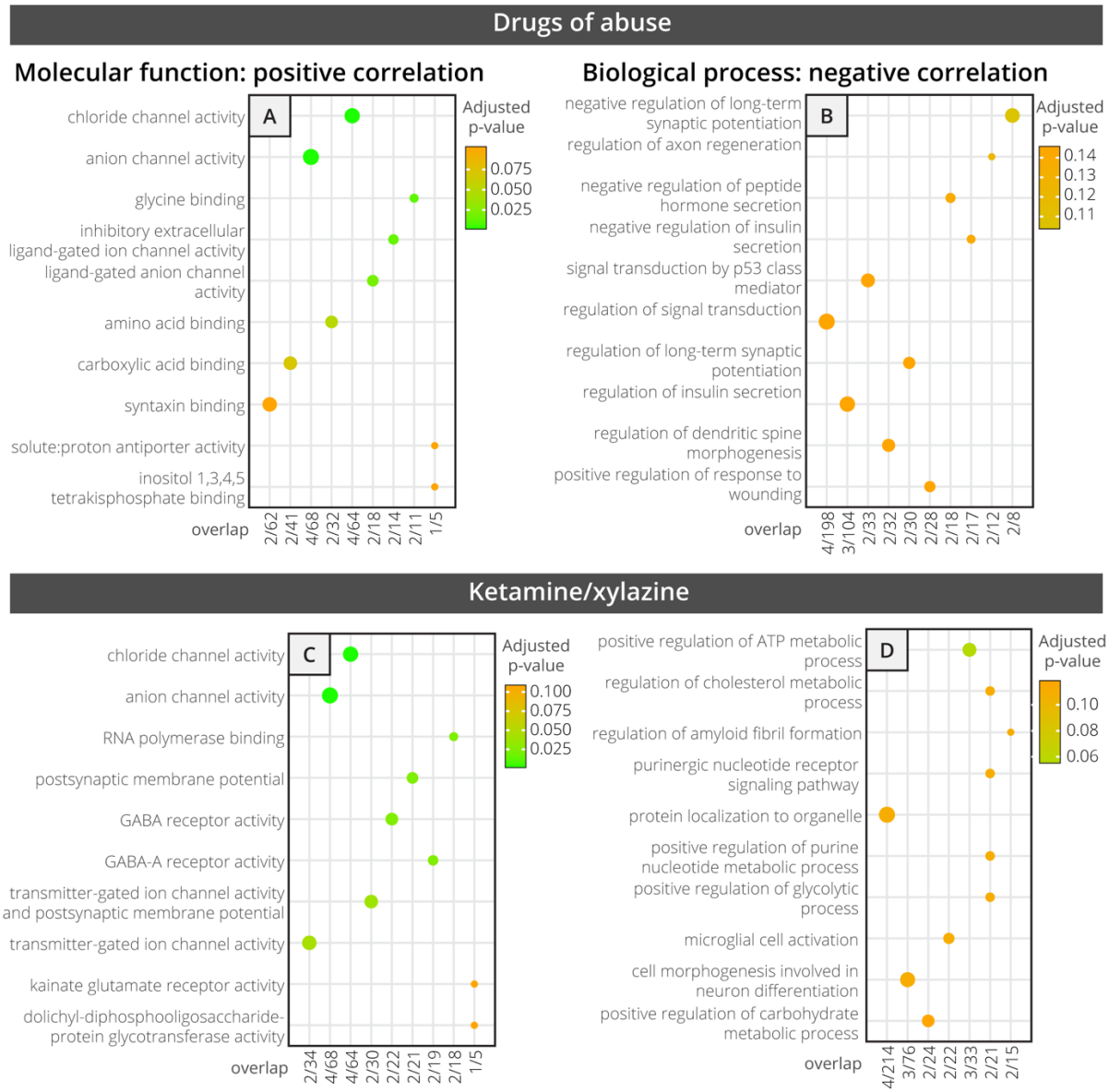

Figure 8: Gene ontology (GO) analysis of top 50 genes within the Allen Gene Expression Atlas correlated with differences in RABV input labeling obtained from experimental vs. control mice.

(A-B) GO from an average of the addictive drug conditions vs. saline-treated controls, all anesthetized using isoflurane.

(C-D) GO from K/X-anesthetized vs. isoflurane-anesthetized saline-treated mice.

Panels A and C show molecular function-related gene classes whose expression was positively correlated with RABV labeling differences, and panels B and D show GO analyses that reflect biological process-related gene classes whose expression was negatively correlated with RABV labeling differences.

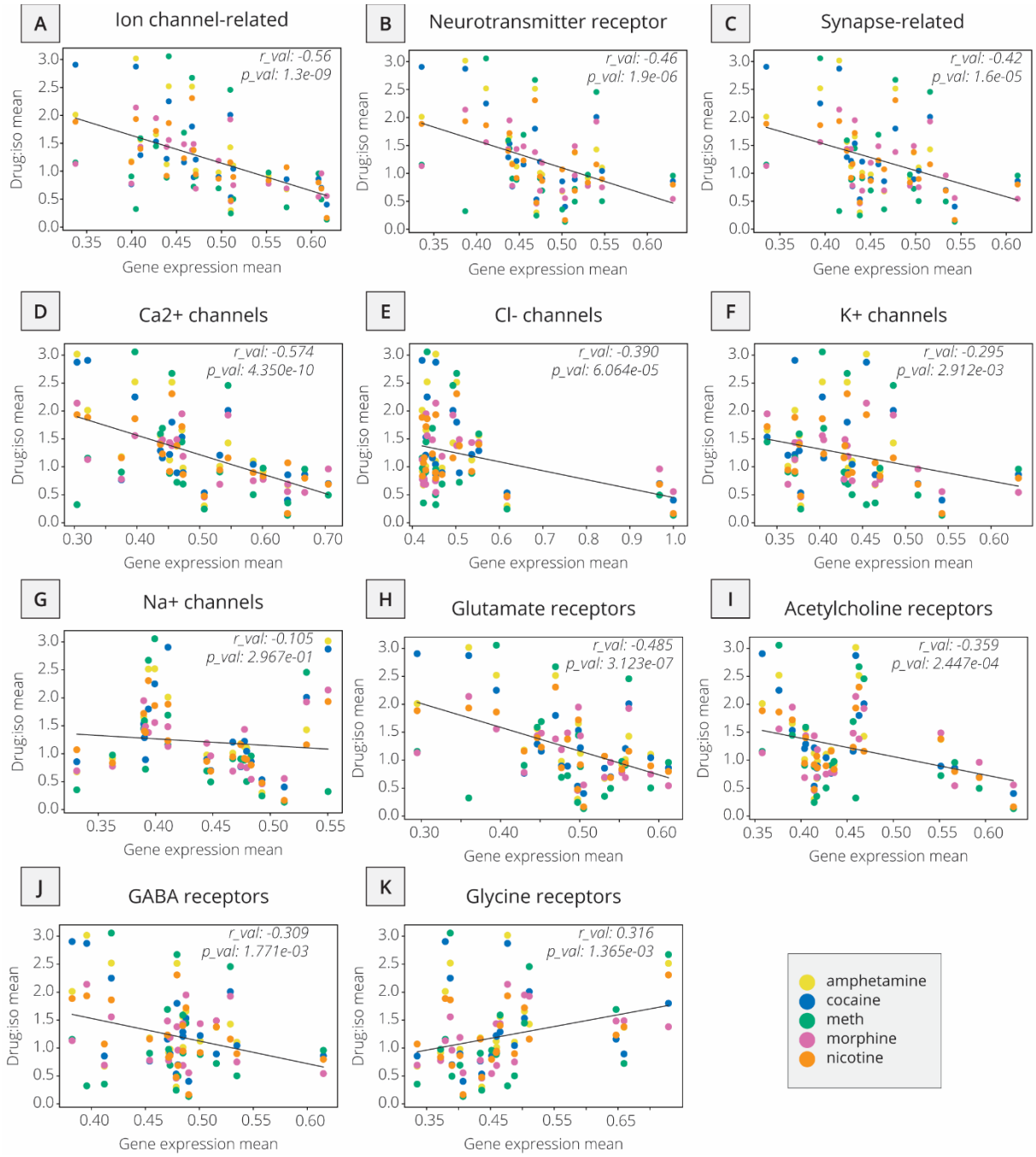

Figure 9: Relationship between RABV labeling ratio in addictive drug/saline-treated groups and mean basal gene expression of gene subgroups, subtypes of ion channels, and neurotransmitter receptors. Linear regressions are shown for all five examined drugs against different gene classes expressed by brain region within the Allen Gene Expression Atlas, including (A) ion channel-related genes, (B) neurotransmitter-related genes, (C) synapse-related genes, (D) Ca^{2+} channels, (E) Cl^{-} channels, (F) K^{+} channels, (G) Na^{+} channels, (H) glutamate receptors, (I) acetylcholine receptors, (J) GABA receptors, (K) glycine receptors.

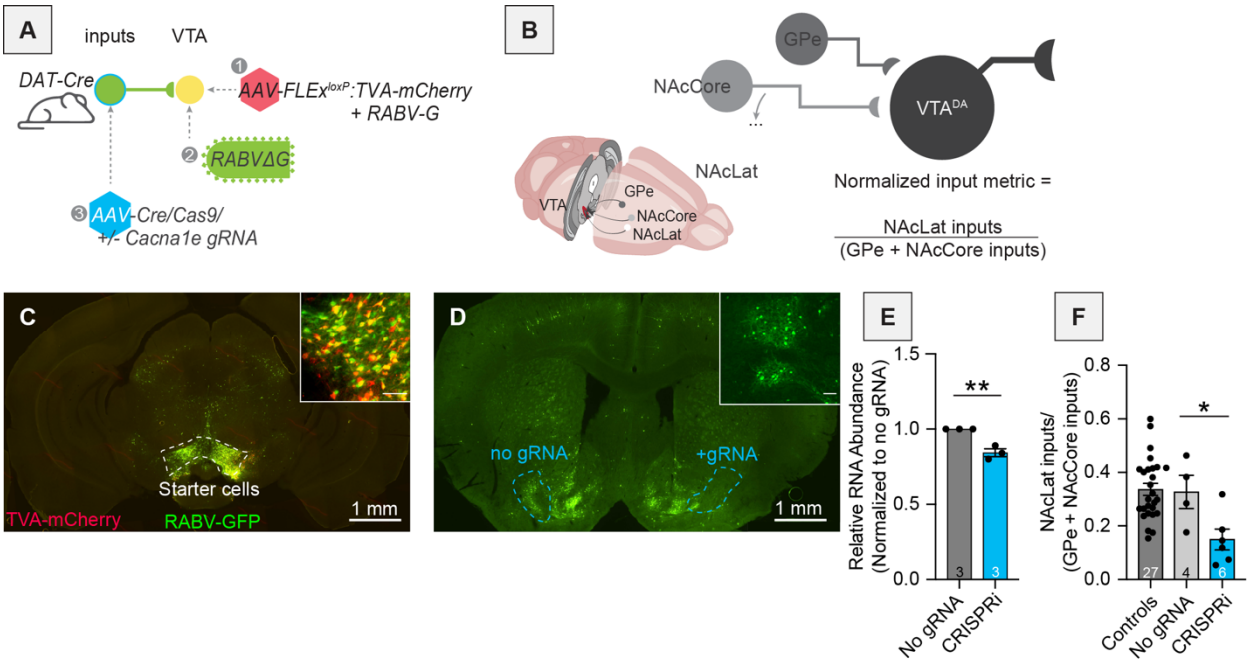

Figure 10: Inhibition of *Cacna1e* expression in the NAcLat reduces RABV-labeled inputs from the NAcLat onto VTA^{DA} cells.

(A) Schematic of viral injections performed.

(B) Schematic of connectivity in relevant brain regions and explanation of the normalized input metric.

(C) Representative image of fluorescence in starter cells in the VTA. Main image scale, 1 mm; inset scale, 100 μm.

(D) Representative image of fluorescence in the NAcLat after either administration of no gRNA (left) or gRNA targeting *Cacna1e* (right). Main image scale, 1 mm; inset scale, 100 μm.

(E) qPCR results showing slight inhibition of *Cacna1e* in the NAcLat.

(F) Difference in RABV-labeled inputs after CRISPRi-mediated knockdown of *Cacna1e* compared to controls[15], and no gRNA. The control conditions are based on previously published data where no AAVs were injected into NAcLat[7].

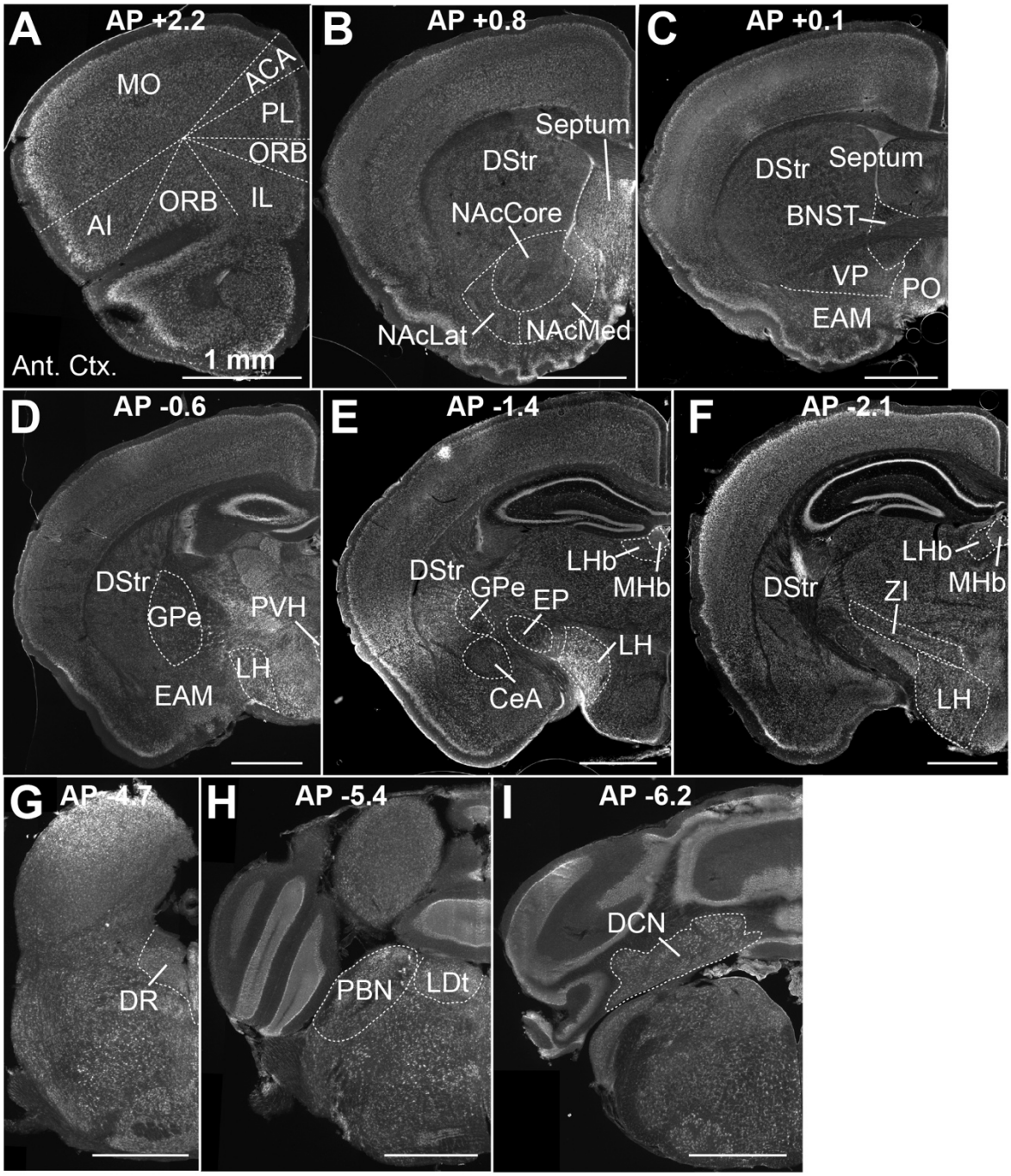

Figure S1: Representative images showing anatomical boundaries for the 22 defined input regions. Each input region is denoted where it is present, and each region is denoted on at least one section.

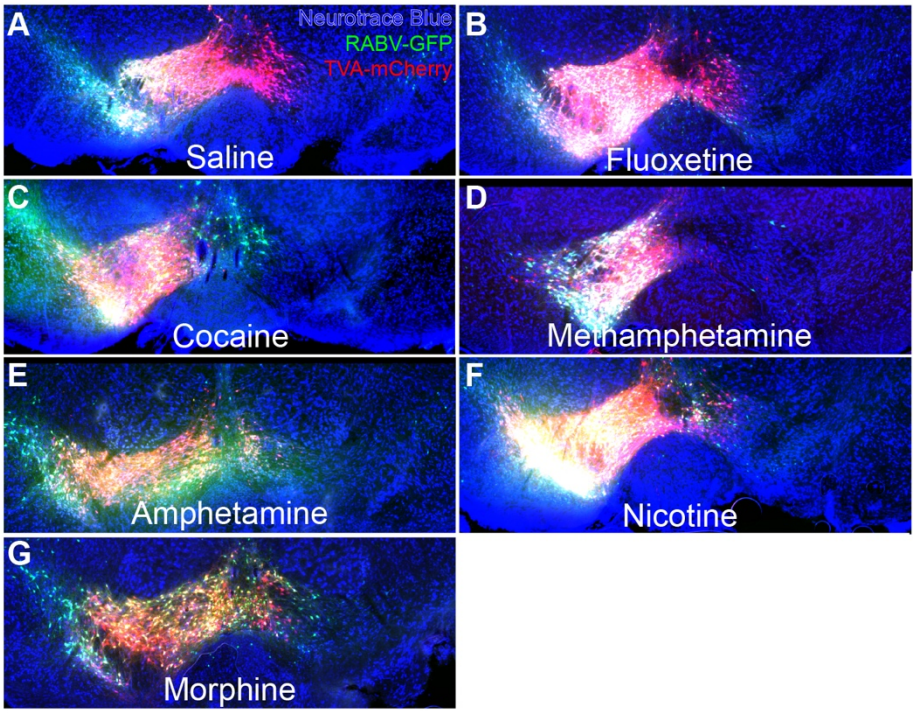

Figure S2: Example images of starter cell distribution from mice in different treatment groups. Red reflects expression of TVA-mCherry; green reflects expression of GFP from RABV; yellow reflects overlap. Related to **Figure 4A**.

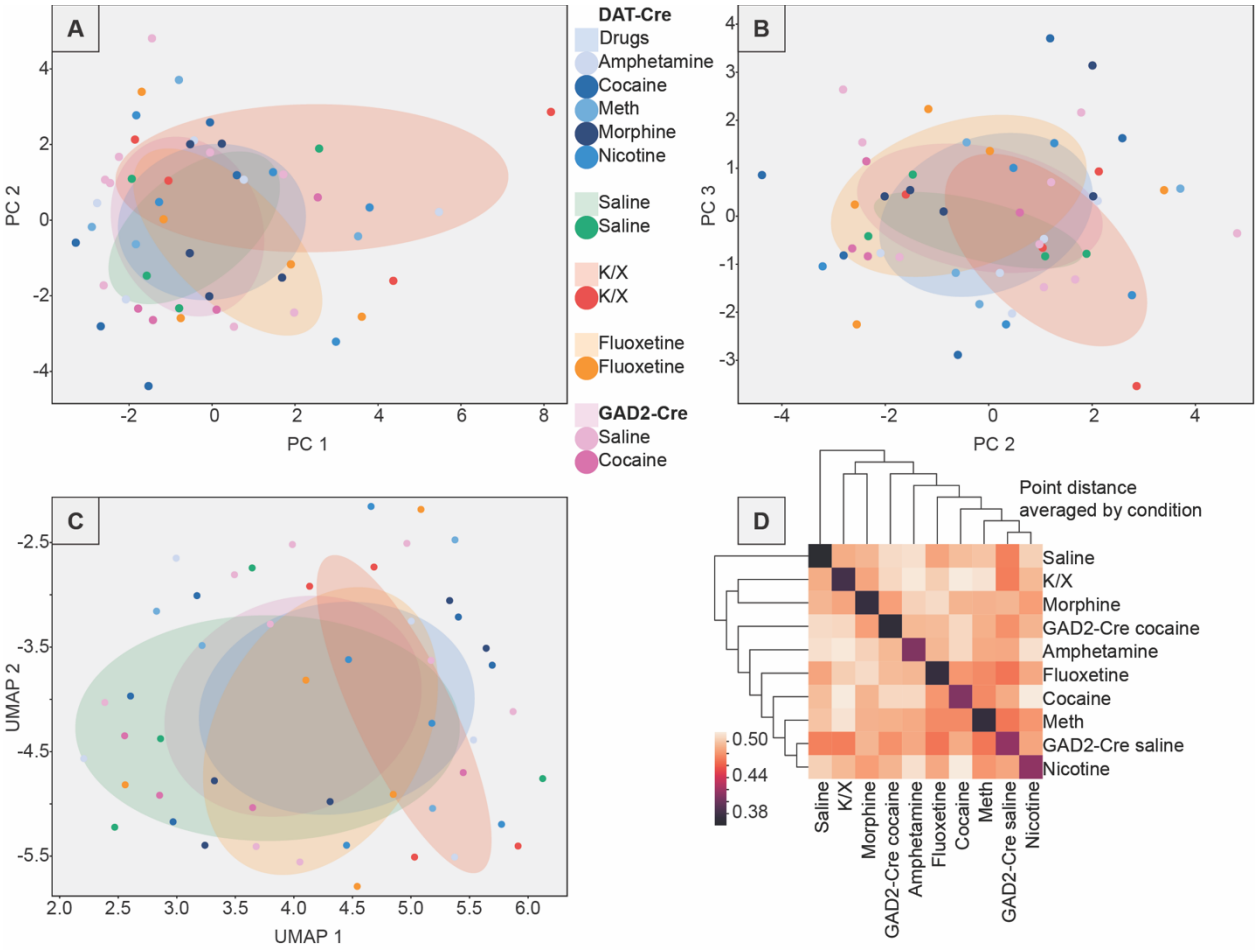

Figure S3: Brains from animals treated with a single exposure to a drug (Figure 5A), but with the brain identities scrambled.

(A) PCA plot showing the data with scrambled identities along PC1 and PC2.

(B) The same scrambled data along PC1 and PC3.

(C) UMAP of the scrambled data.

(D) Correlogram of 20 UMAP embeddings of the scrambled data.

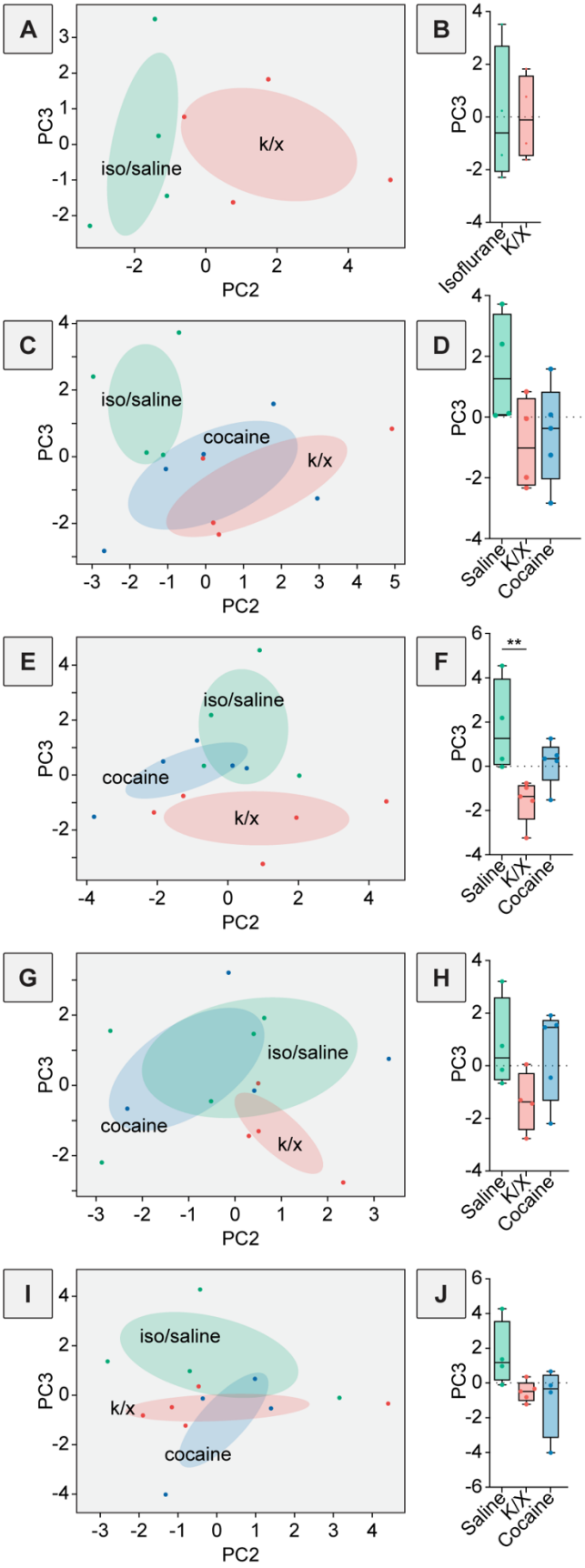
A
B
C
D
E
F
G
H
I
J
PC2
PC3
iso/saline
k/x
cocaine
Isoflurane
Saline
**

1294

1295 **Figure S4: Dimensionality reduction analysis of brains from animals anesthetized with**
1296 **isoflurane and treated with either cocaine or saline, or anesthetized with ketamine/xylazine**
1297 **and treated with saline, focusing on PC3.**
1298 (A) PCA plot of input data from VTA^{DA} cells from mice anesthetized either with isoflurane or K/X
1299 and given saline, showing PC2 and PC3.
1300 (B) Box plot comparisons of PC3, p = 0.99, unpaired t-tests, n = 4 for both.
1301 (C) PCA plot of RABV input mapping experiments to VTA^{DA}→NAcLat cells in mice anesthetized
1302 with isoflurane and given saline or cocaine, or anesthetized with K/X and given saline, showing
1303 PC2 and PC3.
1304 (D) Box plot comparisons of PC3, One-way ANOVA p = 0.12. n=4 for saline and K/X, n = 5 for
1305 cocaine.
1306 (E) PCA plot of input mapping experiments to VTA^{DA}→Amygdala cells, showing PC2 and PC3.
1307 (F) Box plot comparisons of PC3, PC1, One-way ANOVA p = 0.014, pairwise t-tests saline vs.
1308 K/X multiple comparisons adjusted p = 0.011, saline vs. cocaine p = 0.24, K/X vs. cocaine p =
1309 0.16. n = 4 for saline, n = 5 for K/X and cocaine.
1310 (G) PCA plot of input mapping experiments to VTA^{DA}→NAcMed cells, showing PC2 and PC3.
1311 (H) Box plot comparisons of PC3,, One-way ANOVA p = 0.64. PC2, One-way ANOVA p = 0.16,
1312 n = 4 for saline and K/X, n = 5 for cocaine.
1313 (I) PCA plot of input mapping experiments to VTA^{DA}→mPFC cells, showing PC2 and PC3.
1314 (J) Box plot comparisons of PC3, One-way ANOVA p = 0.67. PC2, One-way ANOVA p = 0.083.
1315 n = 4 for saline and cocaine, n = 5 for K/X.

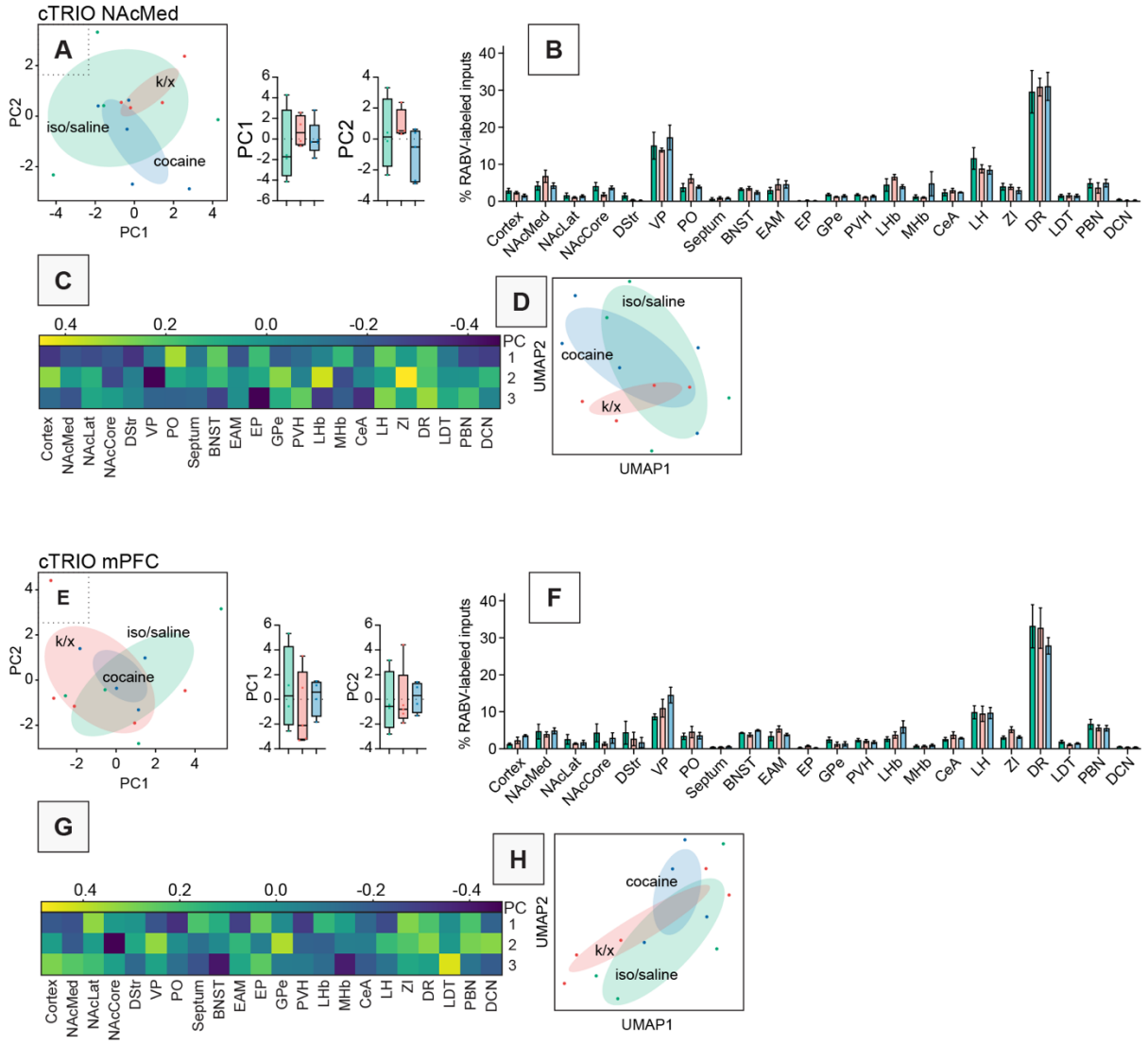

Figure S5: Additional cTRIO data from mice anesthetized with K/X and given saline or isoflurane and given saline or cocaine.

(A) PCA plot of input mapping experiments to VTA^{DA}→NAcMed cells. Box plot comparisons of PC1 and PC2 are shown to the right. PC1, One-way ANOVA p = 0.64. PC2, One-way ANOVA p = 0.27. n=4 for saline and K/X, n = 5 for cocaine.

(B) Bar plot showing percent of RABV-labeled cells in each input region for cTRIO experiments from VTA^{DA}→NAcMed cells.

(C) Heatmap of the contributions of each brain region to PC1 to PC3 for data shown in panel A.

(D) UMAP plot of input mapping experiments to VTA^{DA}→NAcMed cells.

1326 (E) PCA plot of input mapping experiments to VTA^{DA}→mPFC cells. Box plot comparisons of PC1
1327 and PC2 are shown to the right. PC1, One-way ANOVA p = 0.67. PC2, One-way ANOVA p =
1328 0.97. n=4 for saline and cocaine, n = 5 for K/X.
1329 (F) Bar plot showing percent of RABV-labeled cells in each input region for cTRIO experiments
1330 from VTA^{DA}→mPFC cells.
1331 (G) Heatmap of the contributions of each brain region to PC1 to PC3 for data shown in panel E.
1332 (H) UMAP plot of input mapping experiments to VTA^{DA}→mPFC cells.

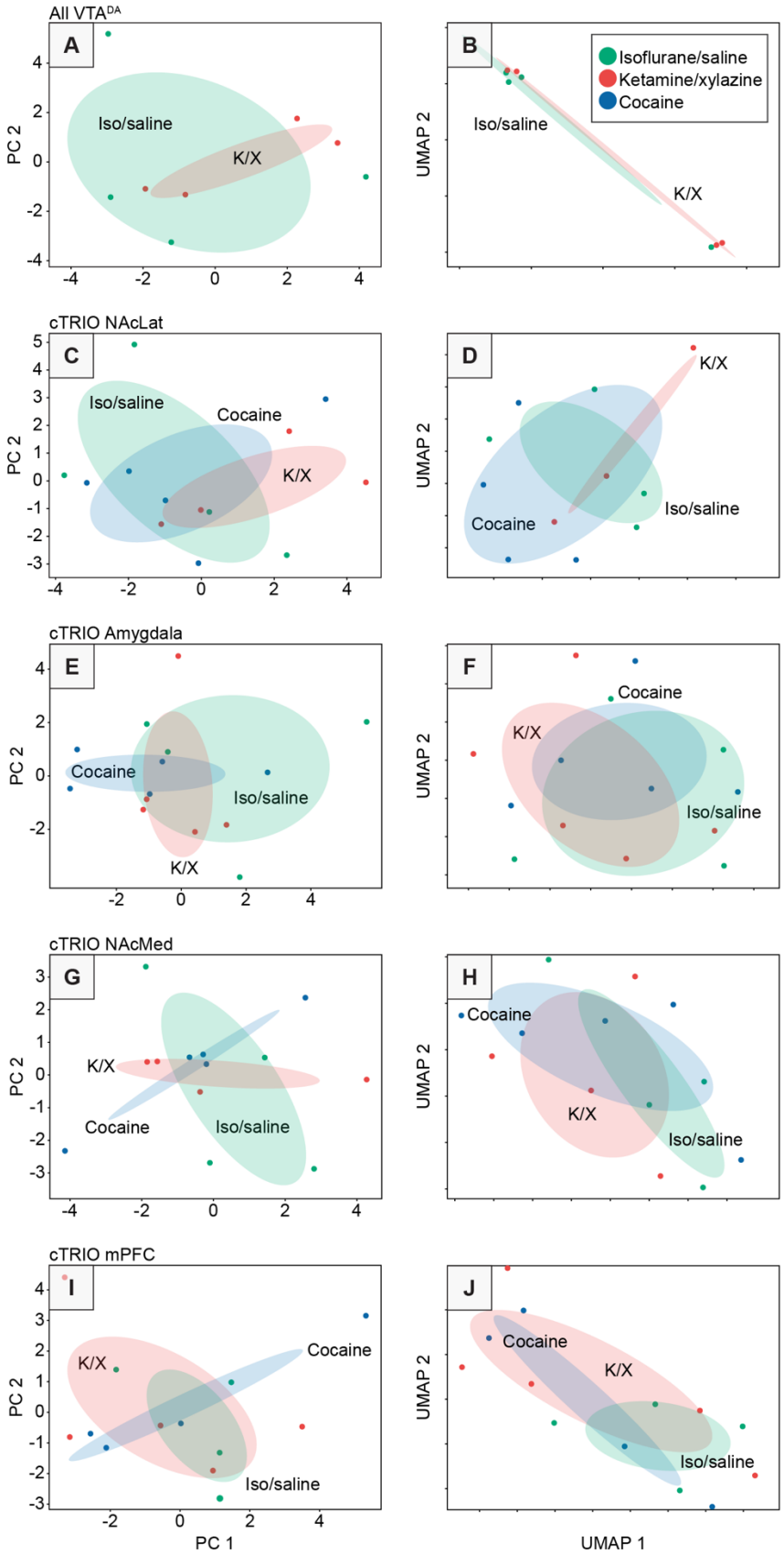
All VTA^DA
A
B
Isoflurane/saline
Ketamine/xylazine
Cocaine
Iso/saline
K/X
PC 2
UMAP 2
cTRIO NAcLat
C
D
Iso/saline
Cocaine
K/X
cTRIO Amygdala
E
F
cTRIO NAcMed
G
H
cTRIO mPFC
I
J
PC 1
UMAP 1

1333

Figure S6: Inputs to brains of mice anesthetized with isoflurane and receiving saline or cocaine, or K/X-saline (Figure 7), but with the brain identities scrambled.

(A) PCA plot of scrambled data from all VTA^{DA} cells including isoflurane-anesthetized and K/X-anesthetized mice.

(B) UMAP plot of scrambled data from all VTA^{DA} cells including isoflurane-anesthetized and K/X-anesthetized mice.

(C) PCA plot of scrambled data from input mapping experiments to VTA^{DA}→NAcLat cells.

(D) UMAP plot of scrambled data from input mapping experiments to VTA^{DA}→NAcLat cells.

(E) PCA plot of scrambled data from input mapping experiments to VTA^{DA}→Amygdala cells.

(F) UMAP plot of scrambled data from input mapping experiments to VTA^{DA}→Amygdala cells.

(G) PCA plot of scrambled data from input mapping experiments to VTA^{DA}→NAcMed cells.

(H) UMAP plot of scrambled data from input mapping experiments to VTA^{DA}→NAcMed cells.

(I) PCA plot of scrambled data from input mapping experiments to VTA^{DA}→mPFC cells.

(J) UMAP plot of scrambled data from input mapping experiments to VTA^{DA}→mPFC cells.

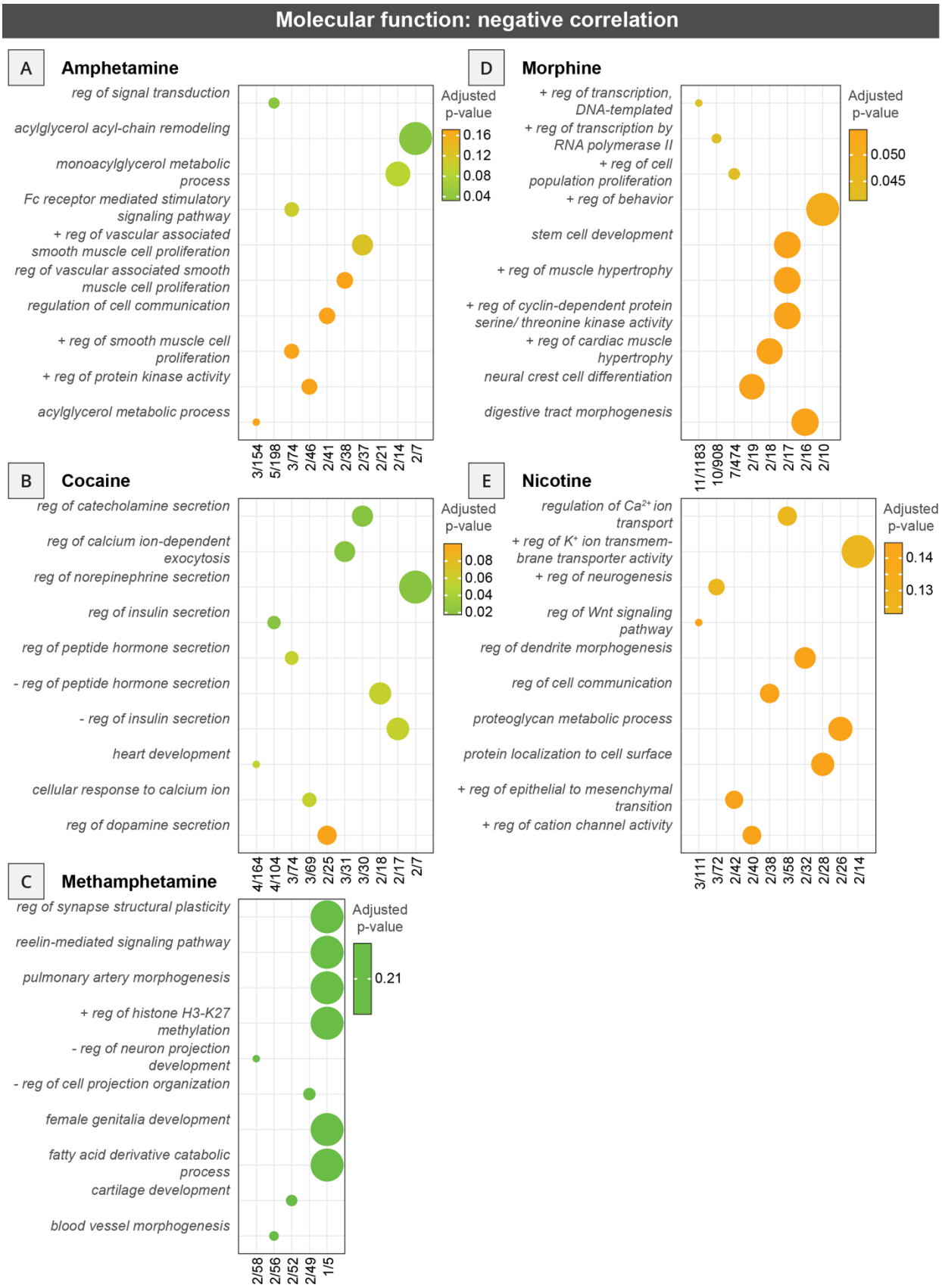
Molecular function: negative correlation
A
Amphetamine
reg of signal transduction
acylglycerol acyl-chain remodeling
monoacylglycerol metabolic process
Fc receptor mediated stimulatory signaling pathway
+ reg of vascular associated smooth muscle cell proliferation
reg of vascular associated smooth muscle cell proliferation
regulation of cell communication
+ reg of smooth muscle cell proliferation
+ reg of protein kinase activity
acylglycerol metabolic process
3/154
5/198
3/74
2/46
2/41
2/38
2/37
2/21
2/14
2/7
Adjusted p-value
0.16
0.12
0.08
0.04
B
Cocaine
reg of catecholamine secretion
reg of calcium ion-dependent exocytosis
reg of norepinephrine secretion
reg of insulin secretion
reg of peptide hormone secretion
- reg of peptide hormone secretion
- reg of insulin secretion
heart development
cellular response to calcium ion
reg of dopamine secretion
4/164
4/104
3/74
3/69
2/25
3/31
3/30
2/18
2/17
2/7
Adjusted p-value
0.08
0.06
0.04
0.02
C
Methamphetamine
reg of synapse structural plasticity
reelin-mediated signaling pathway
pulmonary artery morphogenesis
+ reg of histone H3-K27 methylation
- reg of neuron projection development
- reg of cell projection organization
female genitalia development
fatty acid derivative catabolic process
cartilage development
blood vessel morphogenesis
2/58
2/56
2/52
2/49
1/5
Adjusted p-value
0.21
D
Morphine
+ reg of transcription, DNA-templated
+ reg of transcription by RNA polymerase II
+ reg of cell population proliferation
+ reg of behavior
stem cell development
+ reg of muscle hypertrophy
+ reg of cyclin-dependent protein serine/ threonine kinase activity
+ reg of cardiac muscle hypertrophy
neural crest cell differentiation
digestive tract morphogenesis
11/1183
10/908
7/474
2/19
2/18
2/17
2/16
2/10
Adjusted p-value
0.050
0.045
E
Nicotine
regulation of Ca2+ ion transport
+ reg of K+ ion transmembrane transporter activity
+ reg of neurogenesis
reg of Wnt signaling pathway
reg of dendrite morphogenesis
reg of cell communication
proteoglycan metabolic process
protein localization to cell surface
+ reg of epithelial to mesenchymal transition
+ reg of cation channel activity
3/111
3/72
2/42
2/40
2/38
3/58
2/32
2/28
2/26
2/14
Adjusted p-value
0.14
0.13

1348

1349 **Figure S7: Gene ontology analysis of top 50 expressed genes correlated to differences in**
1350 **RABV input labeling obtained from drug-treated vs. control mice**. GO from mice treated with
1351 (A) amphetamine, (B) cocaine, (C) methamphetamine, (D) morphine, and (E) nicotine-treated
1352 relative to saline-injected controls are shown. Each GO analysis reflects molecular function-
1353 related gene classes whose expression was negatively correlated with RABV labeling differences.

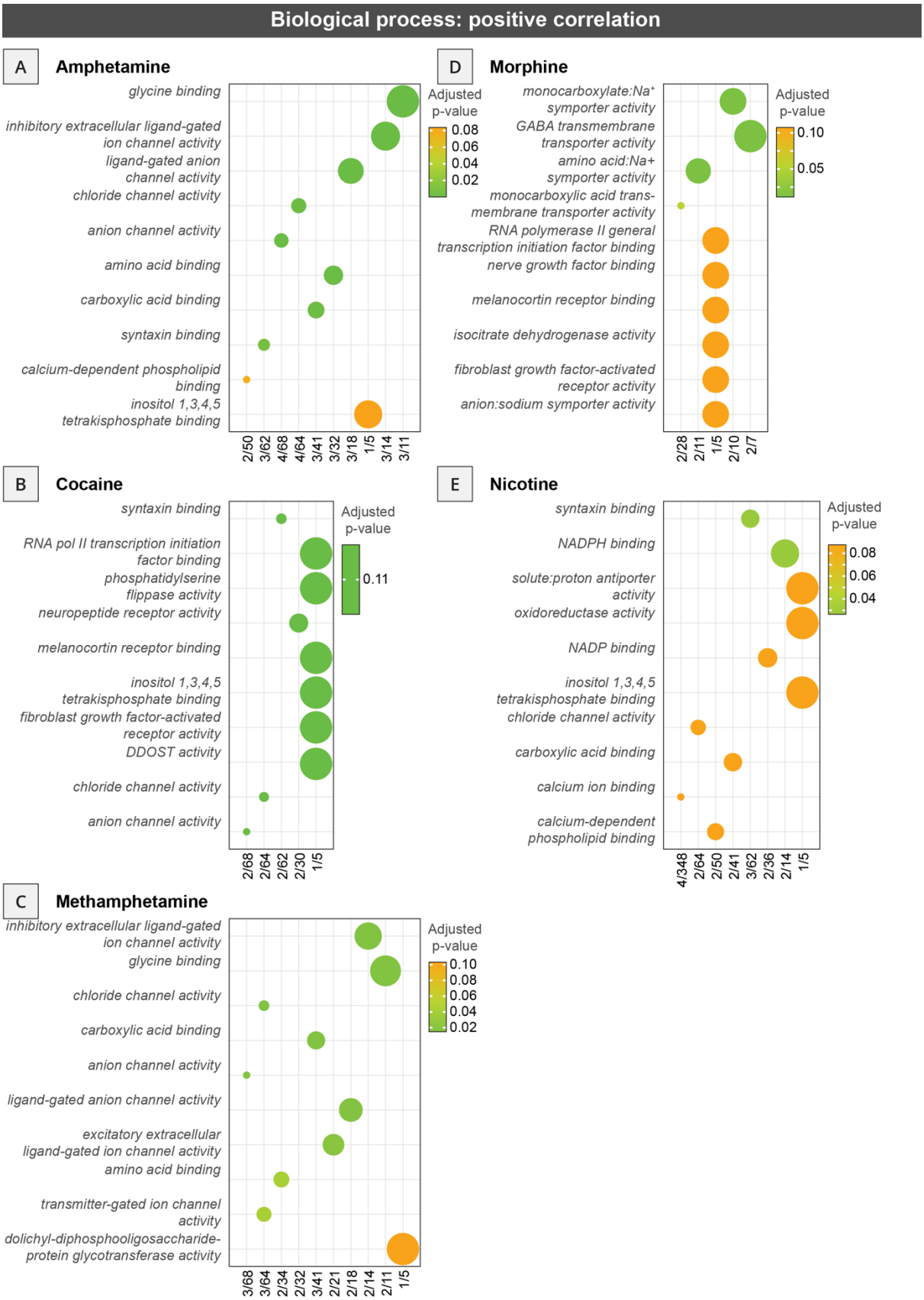
Biological process: positive correlation
A
Amphetamine
glycine binding
inhibitory extracellular ligand-gated ion channel activity
ligand-gated anion channel activity
chloride channel activity
anion channel activity
amino acid binding
carboxylic acid binding
syntaxin binding
calcium-dependent phospholipid binding
inositol 1,3,4,5 tetrakisphosphate binding
2/50 3/62 4/68 4/64 3/41 3/32 3/18 1/5 3/14 3/11
Adjusted p-value
0.08
0.06
0.04
0.02
D
Morphine
monocarboxylate:Na+ symporter activity
GABA transmembrane transporter activity
amino acid:Na+ symporter activity
monocarboxylic acid trans-membrane transporter activity
RNA polymerase II general transcription initiation factor binding
nerve growth factor binding
melanocortin receptor binding
isocitrate dehydrogenase activity
fibroblast growth factor-activated receptor activity
anion:sodium symporter activity
2/28 2/11 1/5 2/10 2/7
Adjusted p-value
0.10
0.05
B
Cocaine
syntaxin binding
RNA pol II transcription initiation factor binding
phosphatidylserine flippase activity
neuropeptide receptor activity
melanocortin receptor binding
inositol 1,3,4,5 tetrakisphosphate binding
fibroblast growth factor-activated receptor activity
DDOST activity
chloride channel activity
anion channel activity
2/68 2/64 2/62 2/30 1/5
Adjusted p-value
0.11
E
Nicotine
syntaxin binding
NADPH binding
solute:proton antiporter activity
oxidoreductase activity
NADP binding
inositol 1,3,4,5 tetrakisphosphate binding
chloride channel activity
carboxylic acid binding
calcium ion binding
calcium-dependent phospholipid binding
4/348 2/64 2/50 2/41 3/62 2/36 2/14 1/5
Adjusted p-value
0.08
0.06
0.04
C
Methamphetamine
inhibitory extracellular ligand-gated ion channel activity
glycine binding
chloride channel activity
carboxylic acid binding
anion channel activity
ligand-gated anion channel activity
excitatory extracellular ligand-gated ion channel activity
amino acid binding
transmitter-gated ion channel activity
dolichyl-diphosphooligosaccharide-protein glycotransferase activity
3/68 3/64 2/34 2/32 3/41 2/21 2/18 2/14 2/11 1/5
Adjusted p-value
0.10
0.08
0.06
0.04
0.02

1354

1355 **Figure S8: Gene ontology analysis of top 50 expressed genes correlated to differences in**
1356 **RABV input labeling obtained from drug-treated vs. control mice**. GO analyses from mice
1357 treated with (A) amphetamine, (B) cocaine, (C) methamphetamine, (D) morphine, and (E)
1358 nicotine-treated relative to saline-injected controls are shown. Each GO analysis reflects
1359 biological process-related gene classes whose expression was positively correlated with RABV
1360 labeling differences.

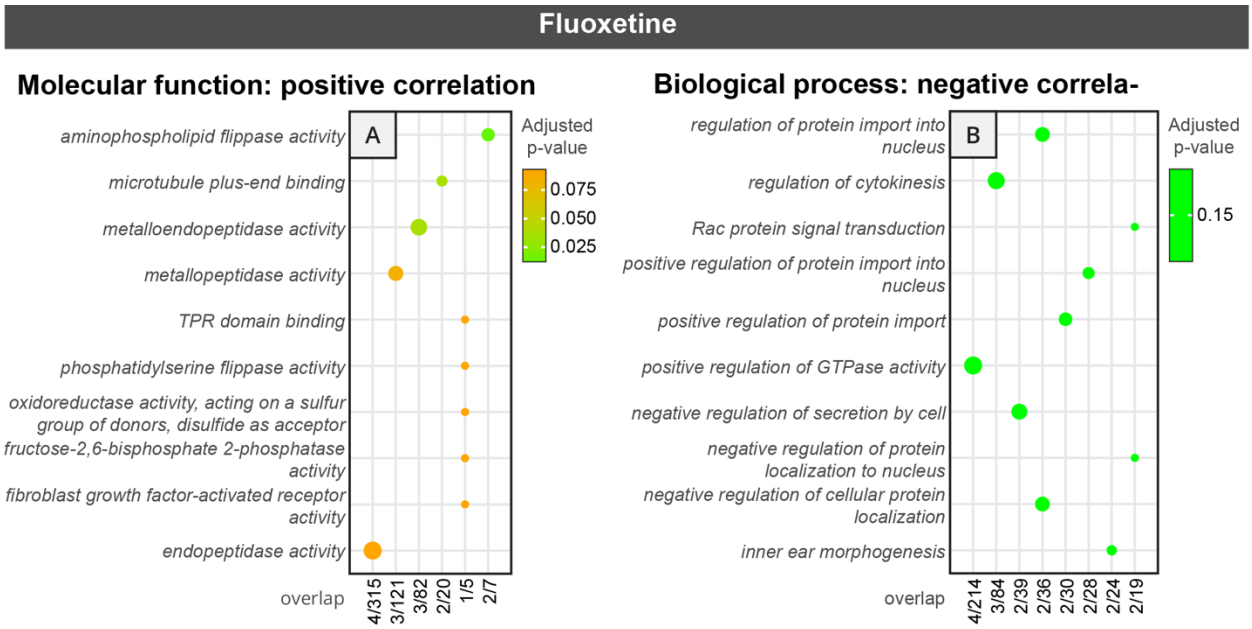

Figure S9: Gene ontology analysis of the top 50 genes correlated with differences in RABV input labeling obtained from fluoxetine vs. saline-treated controls. Panel (A) shows molecular function-related gene classes whose expression was positively correlated with RABV labeling differences, and panel (B) shows GO analyses that reflect biological process-related gene classes whose expression was negatively correlated with RABV labeling differences.

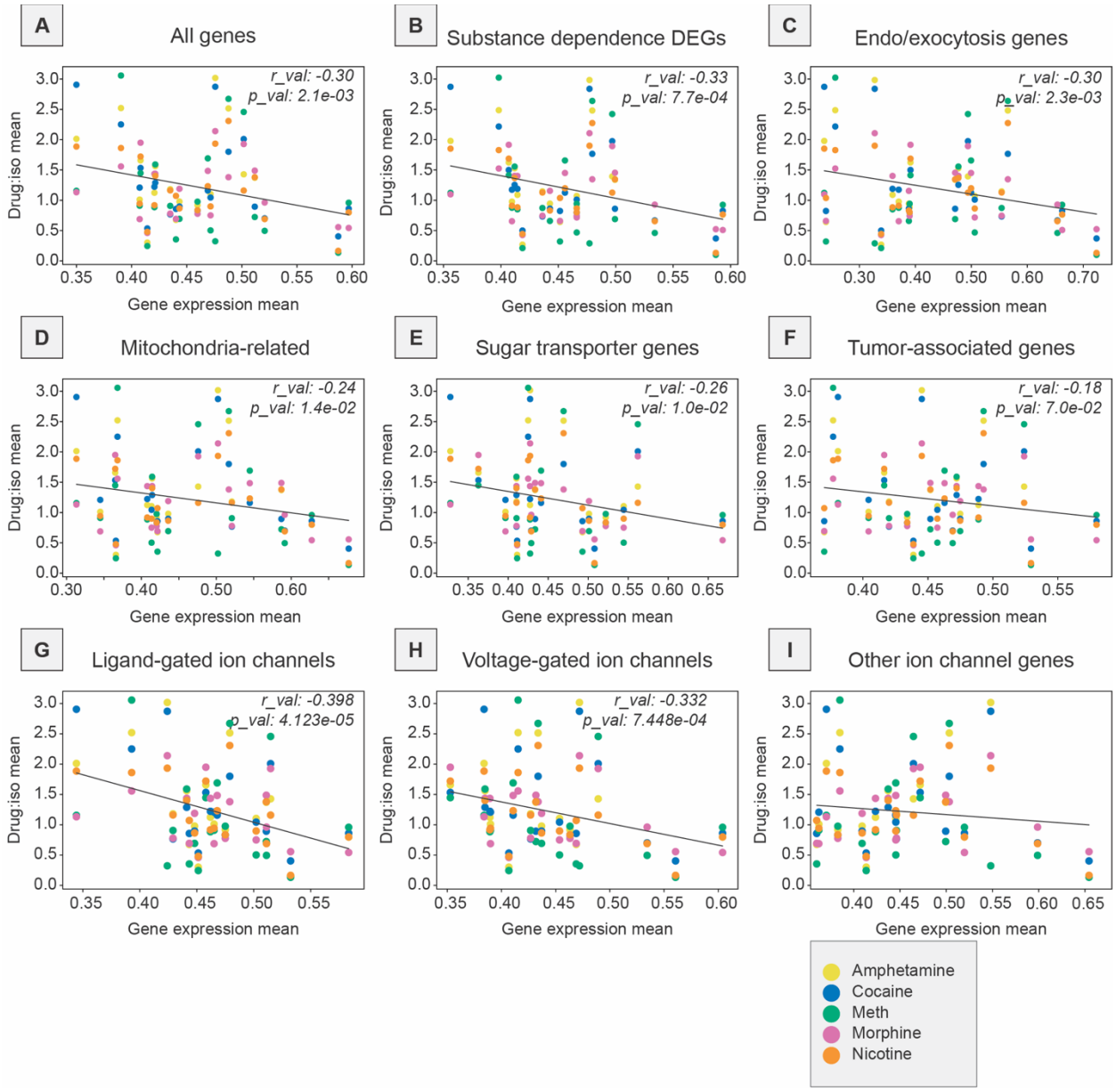

Figure S10: Relationship between RABV labeling ratio in addictive drug/saline-treated groups and mean basal gene expression of gene subgroups. Linear regressions are shown for all five examined drugs against all genes and different gene classes expressed by brain region within the Allen Gene Expression Atlas, including (A) all genes, (B) substance dependence-related genes, (C) endocytosis- and exocytosis-related genes, (D) mitochondrial genes, (E) sugar transporter genes, (F) tumor-associated genes, (G) ligand-gated ion channel genes, (H) voltage-gated ion channel genes, (I) other ion channel genes.

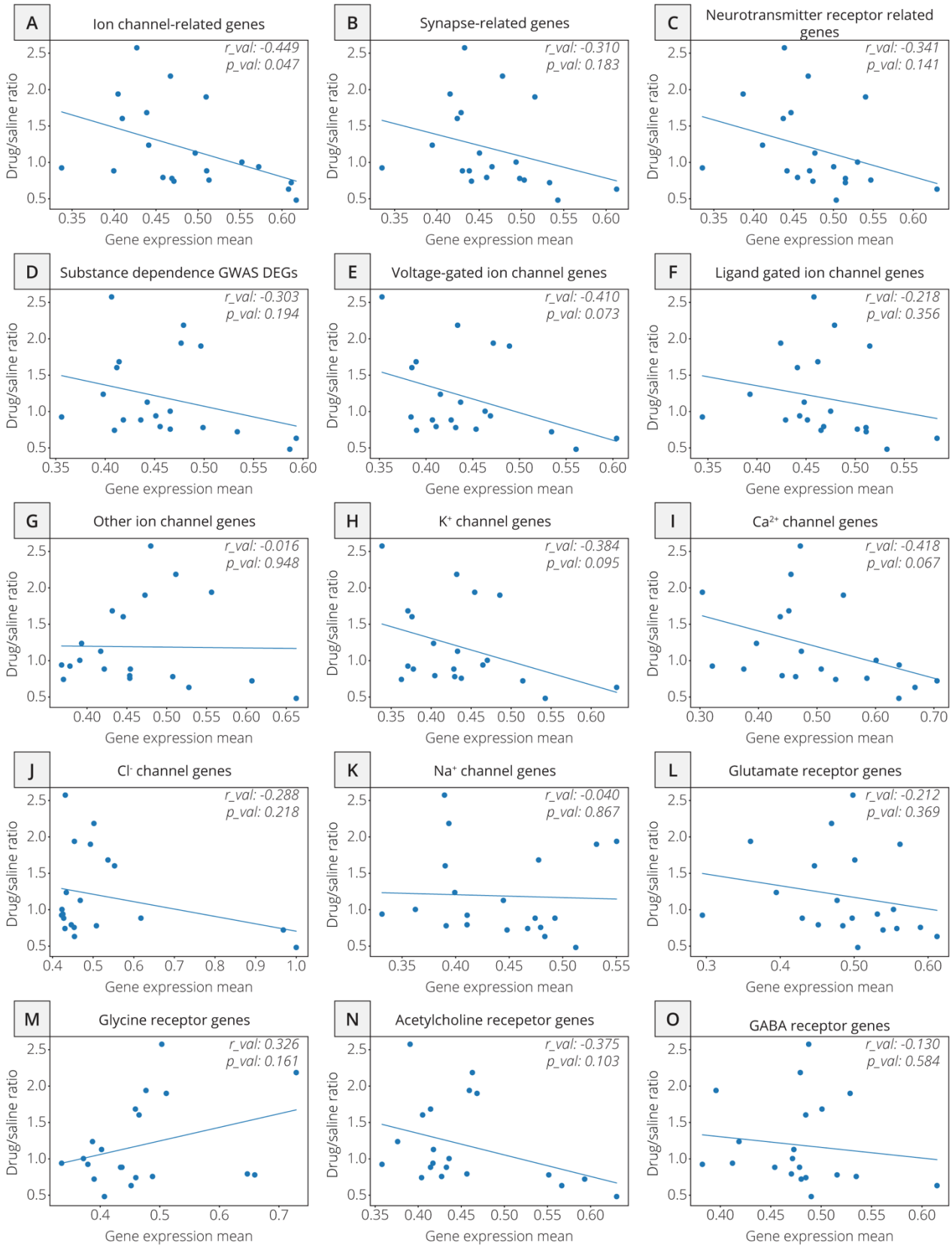
A
Ion channel-related genes
r_val: -0.449
p_val: 0.047
B
Synapse-related genes
r_val: -0.310
p_val: 0.183
C
Neurotransmitter receptor related genes
r_val: -0.341
p_val: 0.141
D
Substance dependence GWAS DEGs
r_val: -0.303
p_val: 0.194
E
Voltage-gated ion channel genes
r_val: -0.410
p_val: 0.073
F
Ligand gated ion channel genes
r_val: -0.218
p_val: 0.356
G
Other ion channel genes
r_val: -0.016
p_val: 0.948
H
K⁺ channel genes
r_val: -0.384
p_val: 0.095
I
Ca²⁺ channel genes
r_val: -0.418
p_val: 0.067
J
Cl⁻ channel genes
r_val: -0.288
p_val: 0.218
K
Na⁺ channel genes
r_val: -0.040
p_val: 0.867
L
Glutamate receptor genes
r_val: -0.212
p_val: 0.369
M
Glycine receptor genes
r_val: 0.326
p_val: 0.161
N
Acetylcholine recepetor genes
r_val: -0.375
p_val: 0.103
O
GABA receptor genes
r_val: -0.130
p_val: 0.584
Drug/saline ratio
Gene expression mean

1375

1376 **Figure S11: Relationship between RABV labeling ratio in K/X-saline vs. isoflurane-saline**
1377 **groups and mean basal gene expression of gene subgroups.** Linear regressions are shown
1378 for K/X-saline vs. isoflurane-saline groups against different gene classes, including (A) ion
1379 channel-related genes, (B) synapse-related genes, (C) neurotransmitter-related genes, (D) DEGs
1380 related to substance misuse, (E) voltage-gated ion channels, (F) ligand-gated ion channels, (G)
1381 other ion channels, (H) K^+ channels, (I) Ca^{2+} channels, (J) Cl^- channels, (K) Na^+ channels, (L)
1382 glutamate receptors, (M) glycine receptors, (N) acetylcholine receptors, (O) GABA receptor genes.

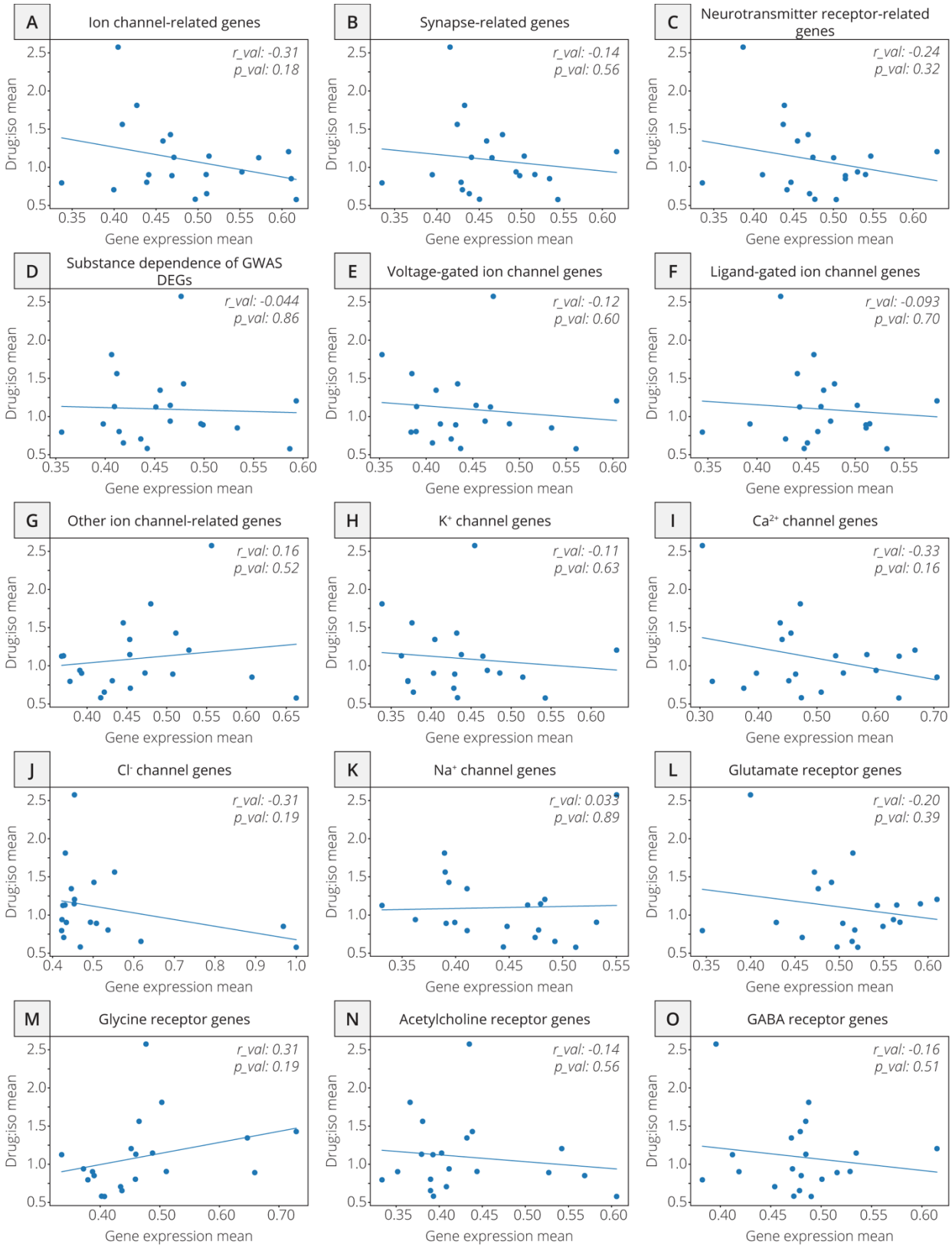
A
Ion channel-related genes
r_val: -0.31
p_val: 0.18
B
Synapse-related genes
r_val: -0.14
p_val: 0.56
C
Neurotransmitter receptor-related genes
r_val: -0.24
p_val: 0.32
D
Substance dependence of GWAS DEGs
r_val: -0.044
p_val: 0.86
E
Voltage-gated ion channel genes
r_val: -0.12
p_val: 0.60
F
Ligand-gated ion channel genes
r_val: -0.093
p_val: 0.70
G
Other ion channel-related genes
r_val: 0.16
p_val: 0.52
H
K⁺ channel genes
r_val: -0.11
p_val: 0.63
I
Ca²⁺ channel genes
r_val: -0.33
p_val: 0.16
J
Cl⁻ channel genes
r_val: -0.31
p_val: 0.19
K
Na⁺ channel genes
r_val: 0.033
p_val: 0.89
L
Glutamate receptor genes
r_val: -0.20
p_val: 0.39
M
Glycine receptor genes
r_val: 0.31
p_val: 0.19
N
Acetylcholine receptor genes
r_val: -0.14
p_val: 0.56
O
GABA receptor genes
r_val: -0.16
p_val: 0.51
Drug:iso mean
Gene expression mean

1383

1384 **Figure S12: Relationship between RABV ratio labeling in fluoxetine vs. saline-treated**
1385 **groups, both anesthetized with isoflurane, and mean basal gene expression of gene**
1386 **subgroups.** Linear regressions are shown for fluoxetine/saline-treated groups against different
1387 gene classes, including (A) ion channel-related genes, (B) synapse-related genes, (C)
1388 neurotransmitter-related genes, (D) DEGs related to substance misuse, (E) voltage-gated ion
1389 channels, (F) ligand-gated ion channels, (G) other ion channels, (H) K^+ channels, (I) Ca^{2+}
1390 channels, (J) Cl^- channels, (K) Na^+ channels, (L) glutamate receptors, (M) glycine receptors, (N)
1391 acetylcholine receptors, (O) GABA receptor genes.

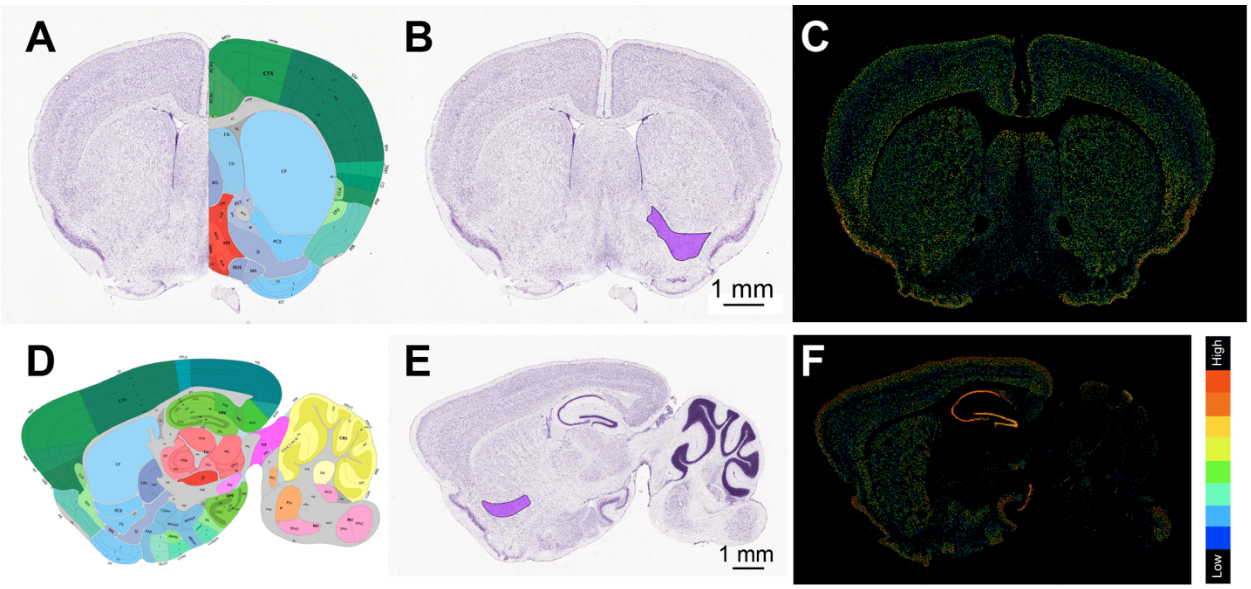

Figure S13: Atlas and AGEA data showing expression of *Cacna1e*. Shown are both coronal (**A-C**) and parasagittal (**D-F**) sections. The NAc is highlighted in panels B and E. The colors in panels C and F reflect the expression energy of *Cacna1e*; the color bar is shown to the right of panel F. Expression of *Cacna1e* is relatively uniform and high throughout the striatum, including the NAc. Imags are from the Allen Mouse Brain Reference Atlas, and *in situ* hybridization/AGEA data from [37].